Global and Planetary Change 192 (2020) 103249

Contents lists available at ScienceDirect

Global and Planetary Change

journal homepage: www.elsevier.com/locate/gloplacha

Uncertainty in temperature and sea level datasets for the Pleistocene glacial cycles: Implications for thermal state of the subsea sediments

Valentina V. Malakhova[a], Alexey V. Eliseev[b,c,d,*]

[a] Institute of Computational Mathematics and Mathematical Geophysics, Siberian Branch of the Russian Academy of Sciences, Novosibirsk, Russia
[b] Lomonosov Moscow State University, Moscow, Russia
[c] A.M. Obukhov Institute of Atmospheric Physics RAS, Moscow, Russia
[d] Kazan Federal University, Kazan, Russia

ARTICLE INFO

Keywords:
Subsea permafrost
Subsea methane hydrates
Glacial cycles
Paleoreconstructions
Response timescales

ABSTRACT

Temperature and sea level changes in the Pleistocene are uncertain. This leads to uncertainty in the associated response of the thermal state of the subsea sediments. We quantified the upper bound of the latter uncertainty in idealised simulations with a model for thermophysical processes in the sediments. At the coast and at the shallow and intermediate–depth shelves and except during relatively isolated time intervals, this bound for permafrost base depth and for the methane hydrate stability zone (MHSZ) characteristics (depth of its bottom boundary and its thickness) is $\leq 45\%$ provided that the geothermal heat flux (GHF) is not larger than 80 mW m^{-2}. These values are much smaller than the uncertainty metrics for the forcing data, which are typically $\geq 65\%$. However, for the intermediate shelf with a larger geothermal heat flux and for the deep shelf irrespective of GHF, different forcing time series may even lead to qualitatively different behaviour of the sediment thermophysical characteristics. We found that prescription of sea level changes plays a crucial role in uncertainty of the simulated subsea permafrost and MHSZ in the deep shelf sediments. In addition, we also quantified uncertainty for estimated apparent response time scales. The relative uncertainty for permafrost base depth and hydrate stability zone thickness time scales is $\leq 20\%$ for most cases. We found no systematic dependence of our results on accounting for millennium–scale temperature variability provided that timescales of the order of 10^4yr are resolved by forcing datasets.

1. Introduction

The Arctic shelf is characterised by a prominent present–day release of methane from the ocean into the atmosphere (Shakhova et al., 2015). It is likely that this release is due to dissociation of the subsea methane hydrates (or, methane clathrates, which is more correct chemical term) (MacDonald, 1990; Buffett, 2000; O'Connor et al., 2010). Such hydrates are stable only at low temperatures or at high pressures. It is of common believe that they formed during the Pleistocene glaciations, when sea level (SL) was below the present–day value by up to 130 m (Fig. S1). This exposed the shelf to very cold (glacial) temperatures (thus, favouring formation of methane hydrates and making the existing methane hydrates more stable) but decreased pressure (hence, making these hydrates less stable). The quantitative data for temperature conditions at the Arctic shelf during Pleistocene glaciations are scarce, but during the Last Glacial Maximum (LGM; circa 21 kyr B.P., before present) mean annual surface air temperature decrease below the present–day values may be as large as 10°C. According to the existing estimates, during glaciations, the temperature effect in methane hydrate stability zone (MHSZ) dominated (MacDonald, 1990; Buffett, 2000; Malakhova and Eliseev, 2017) and led to a widespread extension of the subsea permafrost layers and of MHSZ in the Arctic shelves. In turn, during deglaciation, the Arctic shelf experienced warmer temperatures (arguably similar to the present–day values, which are slightly below 0°C) but with a higher sea water weight–induced pressure. Again, the temperature influence dominated over the pressure one (Malakhova and Eliseev, 2017) resulting in shrinking subsea permafrost and MHSZ. Moreover, different parts of the Arctic shelf with different contemporary seafloor depth H_B were exposed to the air and subsequently flooded at different time instants (Bauch et al., 2001) leading to dependence of the dynamics of the subsea permafrost and MHSZ characteristics on H_B values.

Malakhova and Eliseev (2017) argued that the contemporary methane flux out of the Arctic shelf into the atmosphere is a manifestation

* Corresponding author at: Lomonosov Moscow State University, Moscow, Russia.
E-mail addresses: malax@sscc.ru (V.V. Malakhova), eliseev.alexey.v@gmail.com (A.V. Eliseev).

https://doi.org/10.1016/j.gloplacha.2020.103249
Received 30 March 2019; Received in revised form 4 December 2019; Accepted 1 June 2020
Available online 16 June 2020
0921-8181/

of climate changes between the Pleistocene glacials and interglacials rather than a response to the ongoing climate warming. This consistent with the long, from 5 to 20 kyr, response time scales of the thermophysical properties in thick subsea sediments (Romanovskii et al., 2005; Hunter et al., 2013; Malakhova and Eliseev, 2017) and is supported by the evidence for overall stability of methane hydrates at the Arctic shelf during the onset of the Preboreal warm period about 11.5 kyr B.P. (Sowers, 2006; Petrenko et al., 2017). We note that such long time scales and a limited knowledge on thermophysical state of the subsea sediments in the Pleistocene, dictate very long model simulations to study the subsea permafrost and MHSZ dynamics. In particular, at least one complete glacial cycle is needed to obtain a realistic present–day state, at least two complete glacial cycles are necessary to study the subsea permafrost and methane hydrates stability zone during last glacial cycle, etc. (Malakhova and Eliseev, 2017).

There is a large quantitative controversy between different temperature reconstructions for the Pleistocene glacial cycles. For instance, the MARGO (Multiproxy Approach for the Reconstruction of the Glacial Ocean Surface) project reported the uncertainty range of 1.9 ± 1.8 K (MARGO Project Members, 2009) for decrease of the globally averaged annual mean sea surface temperature during the Last Glacial Maximum relative to the preindustrial state. In individual regions, uncertainty is only widened relative to the global mean estimates (Masson-Delmotte et al., 2013, their Table 5.2). For instance, the LGM surface temperature uncertainty is from 4 to 8 K over the East Eurasia shelf as based on the model–data synthesis by Annan and Hargreaves (2013).

This additionally enhances uncertainty in simulations of subsea permafrost and the methane hydrate stability zone, because the reconstructions for more distant past time intervals are no less uncertain than the LGM reconstructions. For instance, two surface temperature reconstructions for the Last (Eemian) Interglacial (Turney and Jones, 2010; McKay et al., 2011) exhibit large (and non–overlapping) uncertainty ranges for global annual mean temperature difference nominally ascribed to 125 kyr B.P. As an aside issue, we note that the difference between their reconstructions ($+1.5 \pm 0.1$ K and $+0.7 \pm 0.6$ K correspondingly) is additionally exacerbated by the choice of different base intervals (late preindustrial Holocene and 1961–1990 CE respectively), and this inflates both the difference between central estimates and the uncertainty range widths. Additional complications arise due to sparse coverage of the proxy data, which sometimes leads even to an uncertain sign of the reconstructed temperature change during the Last Interglacial (Montoya et al., 2000; Otto-Bliesner et al., 2013).

Moreover, heat propagation in the sediment interior is forced directly by temperature changes at the sediment top, T_B. During interglacials, the present–day shelf or even contemporary coastal areas could be partly or completely covered by water. Because water insulates the sediments from the atmosphere, past T_B changes are dependent both on surface air temperature and on sea level. Our knowledge about sea level changes in the Pleistocene is limited as well. For example, the existing datings of present–day shoreline exposure and flooding during the Last Interglacial are uncertain to several kiloyears (Stirling et al., 1998; Thompson and Goldstein, 2005; Past Interglacials Working Group of PAGES, 2016). Different reconstructions for the last–interglacial SL differ between each other by several metres (Kopp et al., 2009; Dutton and Lambeck, 2012). This also hampers simulation of past evolution of the thermophysical properties of the subsea sediments.

Taking into account the aforementioned uncertainty on past temperature and sea level changes, it is relevant to study sensitivity of the subsea sediments response to imposed boundary conditions at the sediment top. Water phase transitions (freezing and melting) together with the dependence of thermophysical properties on the state of the sediments make heat propagation in the sediments a nonlinear phenomenon. The latter would, in principle, lead to a non–trivial behaviour of the subsea sediments thermophysics under prescribed temperature changes and, thus, to dependence on forcing datasets.

In this paper, we make an attempt to quantify such sensitivity in idealised simulations with a model for thermophysical processes in the sediments. We force our model with an ensemble of temperature variations at the sediment top and estimate the respective spread of responses. Despite the small size of our ensemble, the range of the temperature at the sediment top in the forcing datasets is likely wider than tentative range of possible scenarios for past temperature changes. Therefore, our simulations provide an upper bound for uncertainty estimates. We select temperature in the sediment interior, depths of the permafrost vertical boundaries, and depths of the vertical boundaries of the permafrost–associated methane hydrate stability zone as characteristics of the sediment thermophysics. In addition, we also quantify the uncertainty for estimated apparent response time scales. We highlight that, lacking the biogeochemistry module in our model, we do not attempt to quantify an associated uncertainty in methane release from dissociation of the subsea hydrates.

2. The model for thermophysical processes in the sediments

We use the model for heat propagation in the subsea sediments (Denisov et al., 2011; Eliseev et al., 2015; Malakhova and Golubeva, 2016; Malakhova, 2016; Malakhova and Eliseev, 2018). The model solves the one–dimensional equation for heat diffusion in the sediments with an explicit treatment of melting and freezing. This equation is solved subject to boundary conditions for temperature at the top of the sediments

$$T|_{z=0} = T_B, \tag{1}$$

and for heat flux at the bottom of the computational domain in the sediments

$$\kappa \frac{\partial T}{\partial z}\bigg|_{z=H_S} = G. \tag{2}$$

Here κ is thermal conductivity, z is vertical coordinate below the sediment top (positive downward) and H_S is depth of the bottom boundary of the computational domain in the sediment column. We set $H_S = 1{,}500$ m. Heat capacity and thermal conductivity depend on the state of the sediments (either frozen or unfrozen). Values of these properties correspond to the temperature diffusivity of $1.06 \times 10^{-6} \mathrm{m^2 s^{-1}}$ in the frozen part of the column and to $0.64 \times 10^{-6} \mathrm{m^2 s^{-1}}$ in the unfrozen one. We assume that sediment pores are filled with water up to their holding capacity. The freezing and melting temperature of water in pores is set to $T_F = -1$°C (Nicolsky et al., 2012; Portnov et al., 2014). We explicitly take into account latent heat of fusion during formation and melting of the pore ice but neglect the respective heat released during dissociation of hydrates. In addition, we ignore the difference of latent heat of fusion between pure ice and hydrates–containing ice. Sediment porosity exponentially decreases downward from the value 0.4 at the top of the sediments with the vertical scale 2500 m (Sclater and Christie, 1980).

The prescribed value of the heat flux from the Earth interior (geothermal heat flux, GHF) in the standard version of the model is $G = 60\,\mathrm{mW\,m^{-2}}$, which is estimated as a typical GHF at the Eurasian shelf out of the rift zones (Davies, 2013). However, because at the Arctic shelf G varies approximately from 40 to above $100\,\mathrm{mW\,m^{-2}}$ (Pollack et al., 1993; Davies, 2013), we repeated all our simulations with three additional values of G: 40, 80, and $100\,\mathrm{mW\,m^{-2}}$.

Model equations are solved by using the sweep method at a discrete vertical grid with a vertical step of 0.5 m. Time stepping scheme is implicit with a time step of 1 mo. We do not resolve annual cycle. Initial temperature distribution is prescribed as

$$T(z_j, t = 0) = T(z_{j-1}, t = 0) + G(z_j - z_{j-1})/\kappa_j.$$

Here subscript j indicates computational level within the sediment

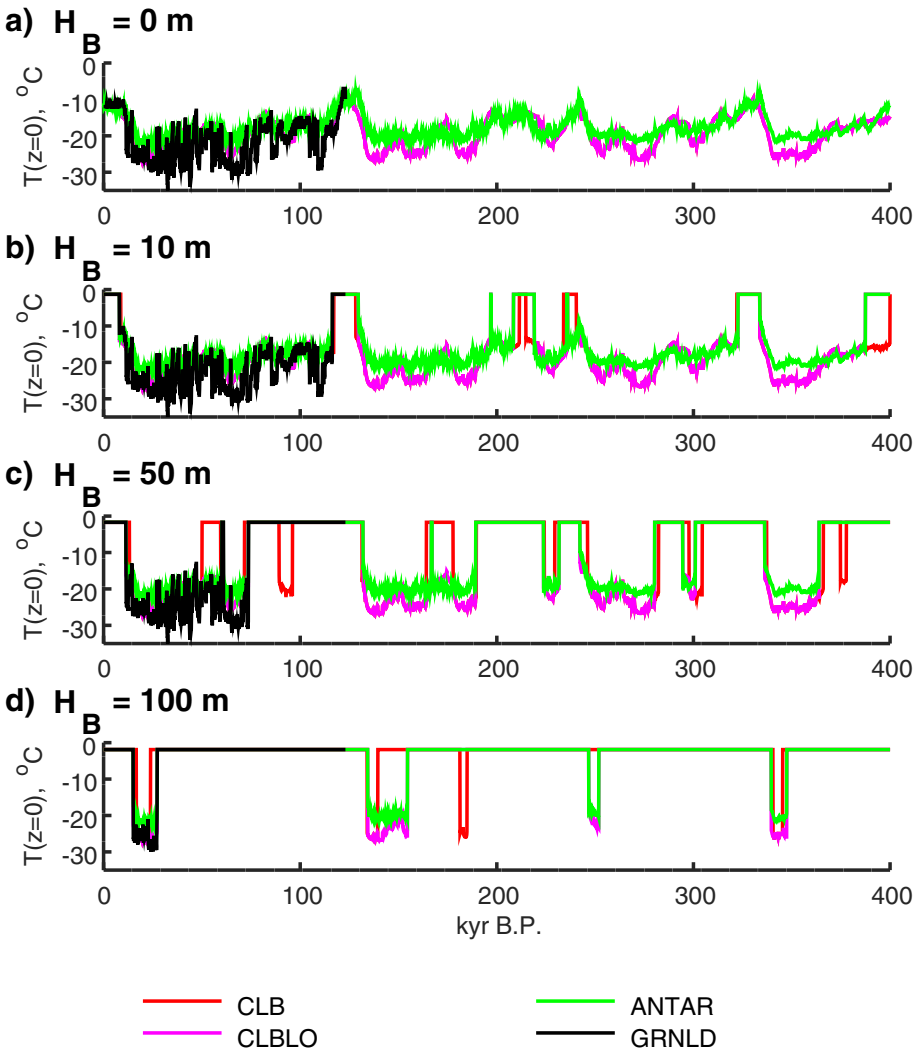

Fig. 1. Temperature at the upper boundary of the sea sediments, which are used to force our model for three values of the contemporary shelf depth H_B. For experiment GRNLD, only last 123 kyr are shown.

(numbered from top to bottom), κ_j is thermal conductivity at this level, and $T(z_0, t = 0) = T_B(t = 0)$. The resulting $T(z, t = 0)$ is almost linear with respect to z. Such profile would be in equilibrium with the specified boundary conditions provided that heat diffusivity is independent from the vertical coordinate. However, because heat diffusivity changes in the vertical direction between frozen and unfrozen layers, we need to spin up the model for 3 kyr.

The equilibrium pressure–temperature curve for methane hydrates is adopted from the TOUGH$^+$HYDRATE model (Reagan and Moridis, 2008). These calculations use formulae as reported in the inlet to Fig. 1 of (Reagan and Moridis, 2008). Salinity of pore water in the sediments is not considered explicitly in the pressure–temperature curve equation. We highlight that we perform our computations only for thermophysical variables and omit the geochemistry completely. Thus, we are unable to estimate methane hydrate stock in the sediments and release of methane from dissociation of these hydrates.

3. Forcing datasets

All numerical experiments were performed for four values of the contemporary isobaths H_B: 0, 10 m, 50 m, and 100 m. Different H_B values lead to different dates of the onsets of shelf flooding during glacial terminations and water withdrawals during development of glaciations (Bauch et al., 2001; Malakhova and Eliseev, 2017). However, the simulations with $H_B = 0$ are not affected by the SL data. The latter simulations may be interpreted as corresponding to the oceanic coast with a caveat that it is not covered by water even if SL is above the contemporary surface. Thereafter, we will refer to the shelf with $H_B = 10$ m as a shallow one, to the shelf with $H_B = 50$ m as an intermediate–depth one, and to the shelf with $H_B = 100$ m as a deep one.

Lacking any meaningful reconstructions for the near–bottom temperature T_B for the Pleistocene, we assume the following simplified scenarios of its change. When the shelf is under water, T_B is set equal to the value corresponding to the near–bottom water temperature $T_{B,w}$. There is a regional scatter in $T_{B,w}$ (Dmitrenko et al., 2011; Nicolsky et al., 2012). To make this scatter tractable in our idealised simulations, we prescribe $T_{B,w}$ as a function of H_B. Namely, we set $T_{B,w} = -1.3^oC$, -1.7^oC, and -1.9^oC for $H_B = 10$ m, 50 m, and 100 m correspondingly (for $H_B = 0$, the value of $T_{B,w}$ is not specified). Similar values for used also by Overduin et al. (2019). In addition, we made simulations with $T_{B,w} \equiv -1.8^oC$. Results of the latter simulations are very similar to those obtained in the main simulations and these simulations are omitted.

When shelf is exposed to the atmosphere, temperature at its top is set equal to the surface air temperature T_a: $T_{B,a} = T_a = T_{a,r} + T_a'$. In this, $T_{a,r} = -12^oC$ is the present–day annual mean surface air temperature at the East Siberian near–shore, and T_a' is a time–varying

Table 1
Combinations of forcing datasets to prescribe temperature anomalies T_a' and sea level.

Run	T_a'	Sea level
ANTAR	EPICA Dome C	(Waelbroeck et al., 2002)
GRNLD	NGRIP for last 123 kyr, EPICA Dome C for earlier period	(Waelbroeck et al., 2002)
CLB	Climber–2	Climber–2
CLBLO	Climber–2	(Waelbroeck et al., 2002)

anomaly obtained from the temperature reconstructions for the Pleistocene.

Time–varying T_a' are prescribed from a handful of available reconstructions (Fig. 1 and Table 1). Malakhova and Eliseev (2017, 2018) derived these anomalies from Vostok borehole data for the last 400 kyr. This dataset is not used in the present paper, because it is superseded by a newer data from the EPICA (The European Project for Ice Coring in Antarctica) Dome C ice drilling program (EPICA Community Members, 2004). These newer data are used to force run ANTAR with our model. In this simulation, sea level was prescribed according to the benthic foraminifera isotopic reconstruction (Waelbroeck et al., 2002).

EPICA temperature data for last glacial cycles are known to lead the proxy–derived global mean temperature by few kiloyears (Shakun et al., 2012) as well as the respective data obtained from the Greenland boreholes (Stocker and Johnsen, 2003; Schmittner et al., 2003; Ganopolski and Roche, 2009; Masson-Delmotte et al., 2013). This motivated us to perform another run, which is thereafter referred to as GRNLD, in which T_a' is prescribed from the NGRIP reconstruction for the last 123 kyr (Kindler et al., 2014). To be confident that initial conditions do not affect our results markedly, we run the model for the last 400 kyr using the EPICA–derived T_a' for time interval from 400 to 123 kyr B.P. Again, SL was prescribed according to (Waelbroeck et al., 2002).

We note that the Greenland reconstruction exhibits the millennium–scale temperature variations with typical magnitude of the order of 10^1K (Fig. 1). Such variations are absent in other utilised here temperature time series. Therefore, it is instructive to study sensitivity of the results with respect to forcing at this timescale.

Then, we used output of the simulation with an Earth system model of intermediate complexity model Climber–2 forced by time–varying orbital parameters and atmospheric CO_2 content (Ganopolski and Calov, 2011). Sea level is directly simulated by this model. For T_a', the data for a grid cell, which corresponding to the East Siberian shelf are selected, and the model present–day multiannual–averaged value is replaced by $T_{a,r}$. This numerical experiment was motivated because Climber–2 simulates larger surface air temperature changes in this grid cell than it is reconstructed from the Antarctic boreholes but smaller than it is derived from the Greenland boreholes (Fig. 1). Below, we refer to this experiment as CLB. As before, the length of this simulation was 400 kyr.

Finally, to test our results to prescription of sea level, we performed another simulation, CLBLO, which was similar to the CLB one but employed the Waelbroeck et al.'s (2002) SL reconstruction in place of the Climber–modelled sea level.

The applied temperature and sea level reconstructions are highly correlated to each other. For instance, the correlation coefficient between two sea level time series is 0.93 for for the last 123 kyr (time interval for which the NGRIP data are available; it approximately covers the last glacial cycle) and is 0.87 for last the 250 kyr (this time interval approximately covers two full glacial cycles and was chosen to remove impact of initial transients (Malakhova and Eliseev, 2017)), see Table S1 and Fig. S1. In general, the fraction of time when the shelf is covered by water is similar between the foraminifera–derived and the Climber–modelled SL (Table S2), while in the latter case this fraction is slightly larger than in the former one. If one considers the intermediate and deep shelves, this fraction is larger for the last 123 kyr than for the last 250 kyr. For shallow shelf, in contrast, the Waelbroeck et al.'s (2002) SL leads to smaller fraction of time with water–covered shelf during the last 123 kyr in comparison to the last 250 kyr, while their Climber–simulated counterparts are almost indistinguishable from each other. As a whole, two SL datasets are in general agreement for interglacials, which is, at least partly, a consequence of defining SL anomalies with respect to the present–day value. During glaciations, however, differences may be as large as 60 m (Table S3 and Fig. S1).

Temperatures obtained from these sources are also correlate to each other (Table S1). However, their values for specific time intervals may differ from each other by 8°C, especially during glacial maxima (Table S4). Among the employed datasets, the annual mean cooling during the Last Glacial Maximum in the EPICA reconstruction is most similar to the pollen–derived estimate for north–east Eurasia (5 to 10°C (Bartlein et al., 2011), Table S4). In turn, both NGRIP and Climber temperatures overestimate this cooling.

Temperatures from different sources employed in the present paper are also highly correlated to both sea level series (Table S1). In addition, while SL generally lags behind surface air temperature which was used to construct T_B, this lag changes in a non–systematic fashion with respect to the choice of time interval from 0 to ≈3 kyr.

4. Uncertainty characteristic

To quantify uncertainty of the simulated variable Y to the choice of forcing datasets, we define mean of over all simulations, $\overline{Y} = K^{-1}\sum_k Y_k$, and intersimulation range $\Delta Y = |\max_k Y_k - \min_k Y_k|$, and introduce the time–dependent ratio

$$r_Y(t) = \Delta Y(t)/\overline{Y}(t).$$

Here K is the total number of simulations ($K = 2$ for SL, $K = 3$ for T_a, $K = 4$ for other variables), and Y_k is the value of Y in simulation k ($1 \le k \le K$), $\max_k Y_k$ and $\min_k Y_k$ are maximum and minimum values of Y with respect to different k. To avoid division by zero in calculating $r_Y(t)$ at time instants when $\overline{Y}(t)$ is close to zero, we replace this time–averaged value by $\max(\overline{Y}(t), Y^{(0)})$, where $Y^{(0)} = 10$ m for sea level, $Y^{(0)} = 1$°C for temperatures, and $Y^{(0)} = 50$ m for depths.

We use the root–mean-square (RMS) value over given time interval

$$R_Y = \mathrm{RMS}(r_Y)$$

to quantify uncertainty of Y for this interval. The root–mean–square option is a compromise between i) the maximum value of r_Y over time interval and ii) value of $r_Y(t)$ averaged over this interval. The first option is too sensitive to localised large spikes of $r_Y(t)$. The second option has too weak sensitivity to large but time–localised values of $r_Y(t)$.

For the last 250 kyr (the last 123 kyr) the RMS uncertainty for sea level is 39% (28%); see Fig. 2 (Fig. S2). The respective uncertainty for T_a is around 79% for both time intervals. For shallow and intermediate shelf, R_{T_B} is ≥45% (Figs. 2 and S2).

We note a subtlety in our approach. Because our model is directly forced by constructed T_B, separate uncertainty measures for SL and T_a should not be misinterpreted. We supplement our plots with uncertainty measures for SL and T_a in addition to such measures for T_B because available paleoreconstructions deliver only separate time series for sea level and surface air temperatures rather than combined T_B. Thus, we need to compare uncertainty measures of the simulated values with the respective measures both for T_B, on one hand, and for SL and T_a, on the other. However, in doing so, we have to bear in mind that uncertainties for the latter two variables should not be over–emphasised, again because the model is only informed by variations of T_B rather than by individual variations of SL and T_a. Nonetheless, it is difficult to formulate rigorously the part of T_B uncertainty which is directly linked to uncertainty in past climate changes. The most difficulties are due to

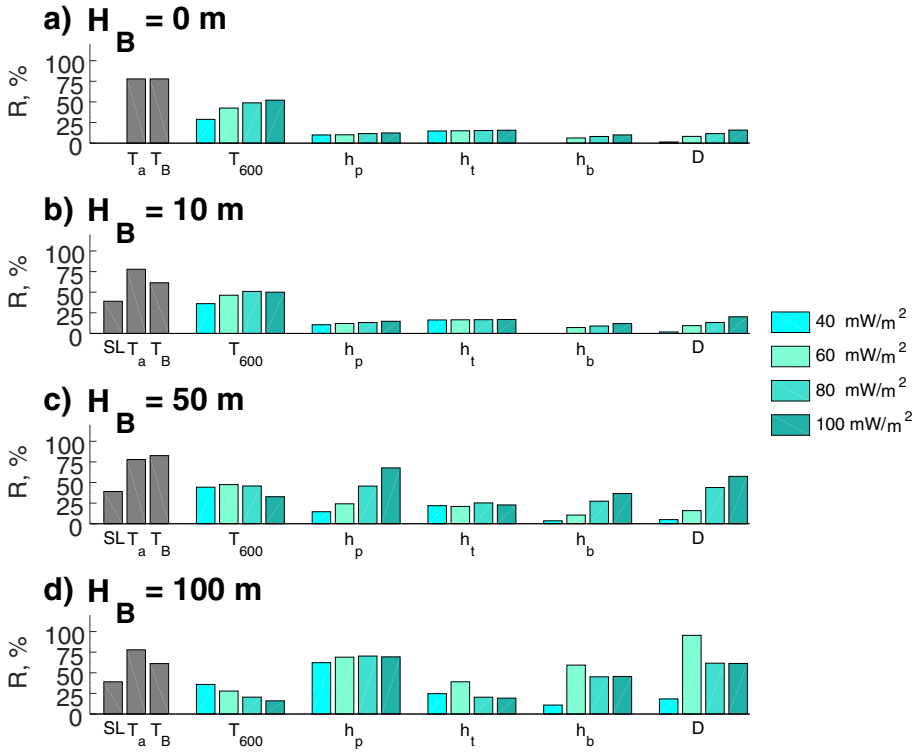

Fig. 2. Root–mean–square uncertainties for input and output variables (gray and cyan bars respectively) for different values of the geothermal heat flux intensity for the last 250 kyr.

- A rigorous estimate of the T_B uncertainty should also include uncertainty to changes in water temperature near the ocean–sediment interface. The latter uncertainty is expected even to dominate when shelf is under deep water layer. However, the values of T_B in this case are basically unknown and may only be somewhat related to the respective present–day values.
- When shelf is at the flooding/exposing time instant, small changes of sea level may lead to large uncertainty in T_B because of complicated interaction between uncertainties in SL and T_a.
- Long time scales of the response of thermophysical properties of subsea sediments to climate variations (Romanovskii et al., 2005; Hunter et al., 2013; Malakhova and Eliseev, 2017) lead to substantially non–local in time relationships between uncertainty in forcing and uncertainty in the simulated thermophysical properties.

As a result, we decided to compare the simulated uncertainties with uncertainties of all T_B, SL, and T_a.

5. Results

5.1. Thermophysical properties of the subsea sediments

The value of temperature at the depth $z = 600$ m, T_{600} (for intermediate values of G, this depth is close to the subsea permafrost base and roughly corresponds to the mid–depth within methane hydrate stability zone), averaged over the last millennium, is not affected strongly by particular choice of T_B (Figs. 3, S4–S6). It differs between different forcing datasets no more than by 1.9°C for $G \leq 40$ W m^{-2} and no more than by 3.4°C for larger G. While the latter difference may look large at first glance, we note that this does not lead to qualitatively different dynamics of permafrost and MHSZ boundaries with respect to different T_B for each studied here value of G (see below). Further back in time, the difference between the model responses to different forcing datasets becomes more pronounced and mostly related to the difference between amplitude of T_B variations among the forcing datasets. In addition, the sea level contribution to response differences between these datasets becomes more pronounced with increasing H_B (cf. CLB and CLBLO, in which the mean T_{600} for 135–125 kyr B.P. is as large as 5.9°C for $G = 100$ W m^{-2}, Fig. S6). In each case, the 'overall signal' (the difference of T_{600} between different time intervals) is not lost when one goes from one forcing dataset to the other.

Geothermal heat flux intensity G strongly affects qualitative results of our simulations. This may be illustrated by comparing T_{600} averaged over the last millennium of simulations for different values of G (Fig. 4). For the coast, and for the shallow and intermediate shelves, the last–millennium T_{600} values are either below or above the freezing point depending on G. However, for any H_B and for each G, the simulated for different T_B uncertainty of T_{600} appears to be sufficiently small to state that the overall signal is qualitatively independent of the choice of particular forcing dataset.

The RMS value $R_{T_{600}}$ for the coast and for the shallow shelves is from 35% to 88% for the last 250 kyr (Fig. 2), which is comparable to the respective values for T_B. Similar results are obtained for the last 123 kyr (Fig. S2). For the intermediate and deep shelves, in turn, the respective value is from 11% to 52% depending on G, which is smaller than its T_B counterpart. For the coast and for the shallow shelf, $R_{T_{600}}$ is much improved if we discard simulation ANTAR (Fig. S3). This again reflects that the differences in T_{600} between the simulations with different forcing datasets are mostly related to the corresponding differences in T_B amplitudes. There are marked differences in RMS uncertainties for T_{600} between simulations with different G. However, they are not systematic: there is a positive correlation of $R_{T_{600}}$ with G for the coast and for the shallow shelf, but a negative one for the deep shelf.

For the depth of the subsea permafrost bottom boundary, h_p, during the last glacial cycle (the last 123 kyr of simulations), the differences between the simulations, which are forced by different datasets, decrease with increasing H_B with the maximum values during the last millennium (Figs. 5, S7–S9). For the deep shelf, the sensitivity of h_p to imposed T_B is high during the time interval around 130 kyr B.P. In this time interval, the difference in the simulated h_p changes from 131 m for

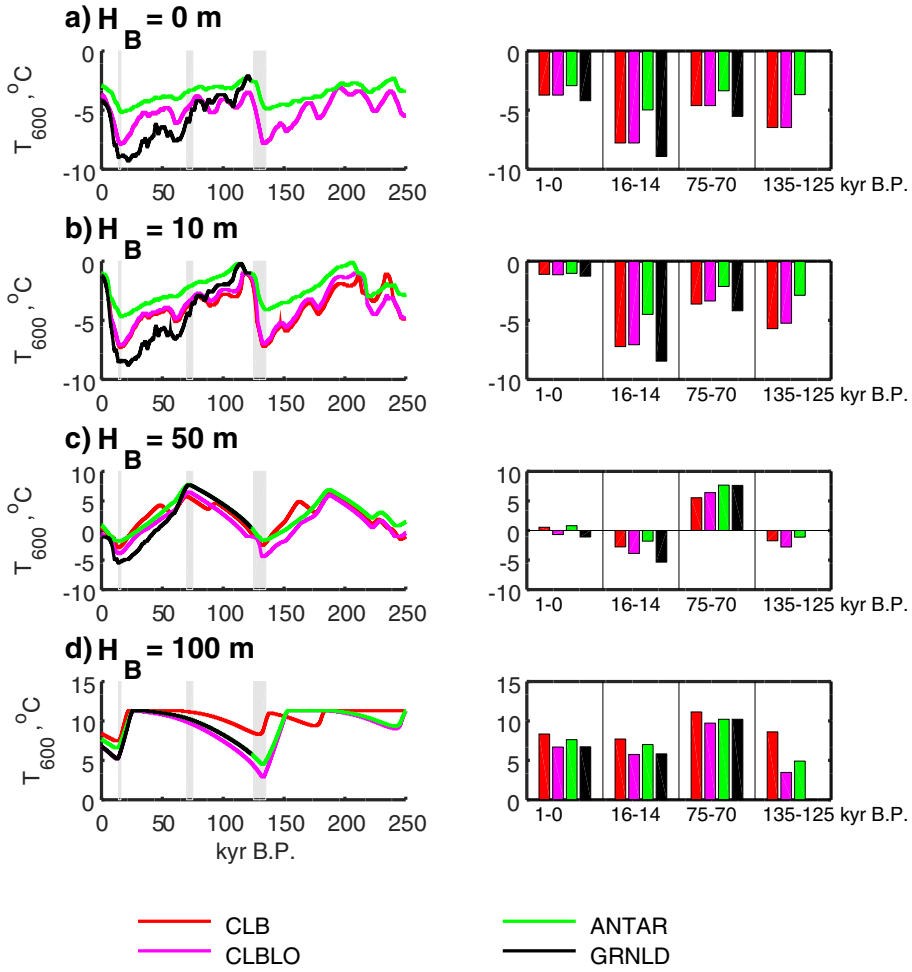

Fig. 3. Temperature at the depth 600 m below the seafloor for four values the contemporary shelf depth H_B for simulations with $G = 60\ \mathrm{mW\,m^{-2}}$. For experiment GRNLD, only last 123 kyr are shown. Right panels show $T(z = 600\ \mathrm{m})$ averaged over specified time intervals. Last three time intervals (from 16 to 14 kyr B.P., from 75 to 70 kyr B.P., and from 135 to 125 kyr B.P.) are also depicted by gray rectangles at right panels.

$G = 100\ \mathrm{W\,m^{-2}}$ to 210 m for $G = 40\ \mathrm{W\,m^{-2}}$, and is mostly caused by differences in the prescribed sea level. For $H_B = 0$ and $H_B = 10$ m, $r_{h_p} \le 20\%$ during the last 250 kyr. For $H_B = 50$ m, it is typically below 50%, except for some isolated time intervals (e.g., around 70 kyr B.P., when it is as large as 75% for $G = 100\ \mathrm{W\,m^{-2}}$).

For all time intervals, absolute uncertainty increases with decreasing G (see Fig. 6 as an example). However, there is a principal difference between the dependencies of absolute and relative uncertainties on G, which is caused by the upward overall shift of the forcing dataset–averaged h_p under stronger heat flux from the Earth interior. This shift, despite of the aforementioned negative correlation between absolute uncertainty of h_p and G, leads to the positive correlation between the respective negative uncertainty and geothermal heat flux intensity. For the coast and for the shallow shelf, R_{h_p} is ≤16% both for the last 250 kyr and for the last 123 kyr — markedly smaller than the respective values for T_B. In contrast, the results of simulations for $H_B = 100$ m are divergent, and r_{h_p} in this case is frequently > 50%. For this shelf depth, R_{h_p} is from 62% to 70% depending on G both for the last 250 kyr and for the last 123 kyr, which is larger than their T_B counterparts. A transition between large and small relative RMS uncertainty occurs at $H_B = 50$ m. At this depth, R_{h_p} is ≤24% for $G \le 60\ \mathrm{mW\,m^{-2}}$, but is as large as 68% for $G = 100\ \mathrm{mW\,m^{-2}}$ and for the last 250 kyr (Fig. 2). Its counterpart for the last 123 kyr is equal to 59% (Fig. S2). Nonetheless, even the largest among different imposed GHF the uncertainty R_{h_p} for $H_B = 50$ m appears to be smaller than R_{T_B} at the same shelf depth.

Depth of the MHSZ upper boundary, h_t, responds rapidly to imposed changes, and, for all H_B values, its value averaged over the last millennium differs between different simulations not larger than by few meters ($r_{ht} \le 4\%$ for each G). However, if one goes back in time, intersimulation range Δh_t increases. For the shallow shelf, the 'overall signal' is distorted by choice of T_B but is not lost. For the intermediate shelf, this 'signal' for CLB and CLBLO markedly deviates from that for ANTAR and GRLND (e.g., around 55 kyr B.P. and around 170 kyr B.P.). We note in this respect that the Climber–simulated excursions of T_B are more important relative to the sea level prescription. Nonetheless, $R_{ht} \le 40\%$ (or even ≤25% for $H_B \le 50$ m) both for the last 250 kyr and for the last 123 kyr. This is smaller than their T_B counterparts.

There is a qualitative similarity between the time dependencies of hydrate stability zone thickness D and of the MHSZ base depth h_b. The same is true for dependencies of D and h_b on G. When D and h_b are averaged over the last millennium of the simulations with each G, their value is constrained at least by 140 m for all values of H_B (Figs. 7, and S10–S12). Both for the last 250 kyr and for the last 123 kyr, $R_{h_b} \le 12\%$ for the coast and for the shallow shelf (Figs. 2 and S2), which is markedly smaller than the corresponding R_{T_B}. For the deep shelf and for both these time intervals, $10\ \% \le R_{h_b} \le 59\%$ and $18\ \% \le R_D \le 95\%$ depending on G. This is typically above the respective values of R_{T_B}. We note that R_D may be underestimated for small GHF (here, it is 40 $\mathrm{W\,m^{-2}}$) because in this case MHSZ base is located at the lower boundary of our computational domain, and RMS uncertainty for D is only due to its counterpart for h_b. Nonetheless, a systematic dependence

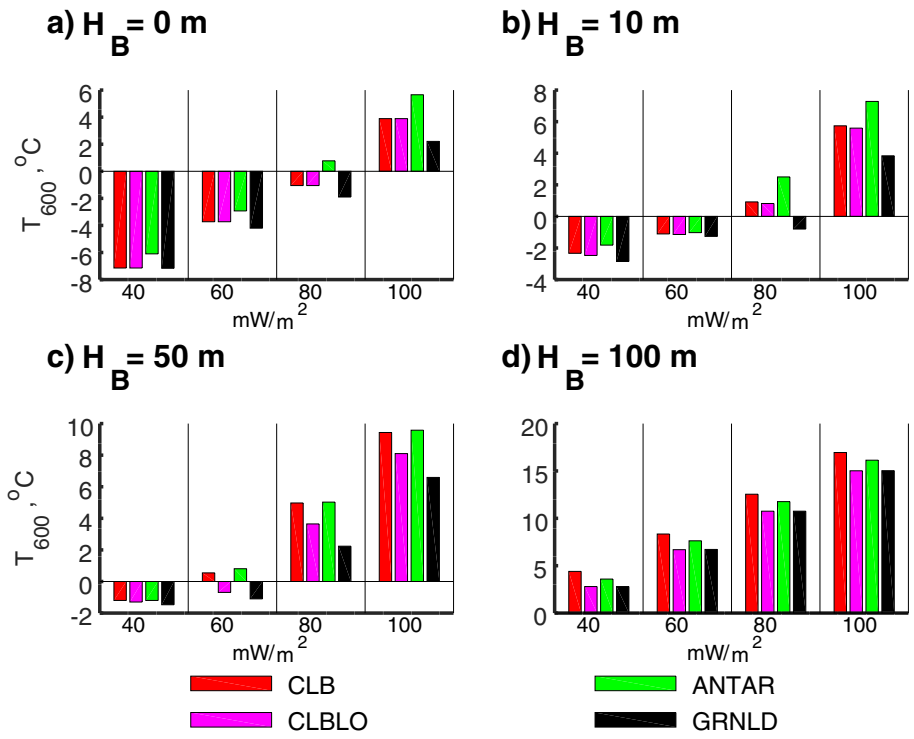

Fig. 4. Temperature at the depth 600 m below the seafloor averaged over the last millennium of the simulations with different values of the geothermal heat flux intensity *G*.

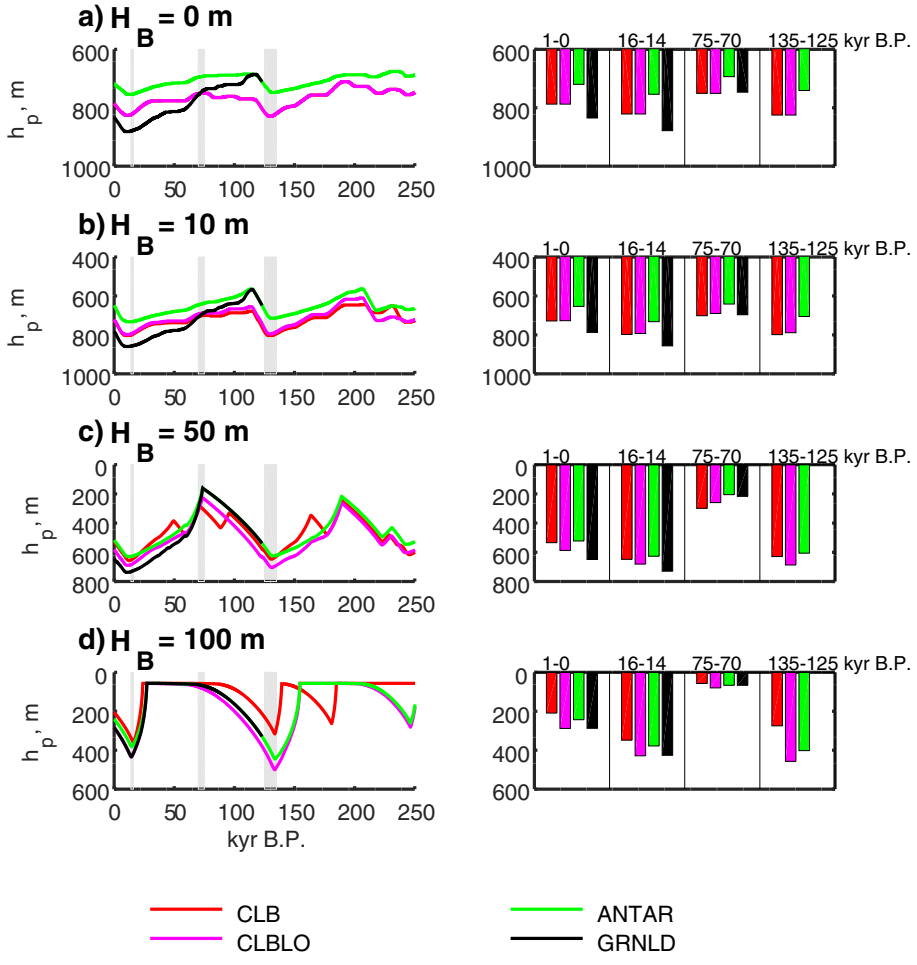

Fig. 5. Similar to Fig. 3 but for depth of the permafrost base.

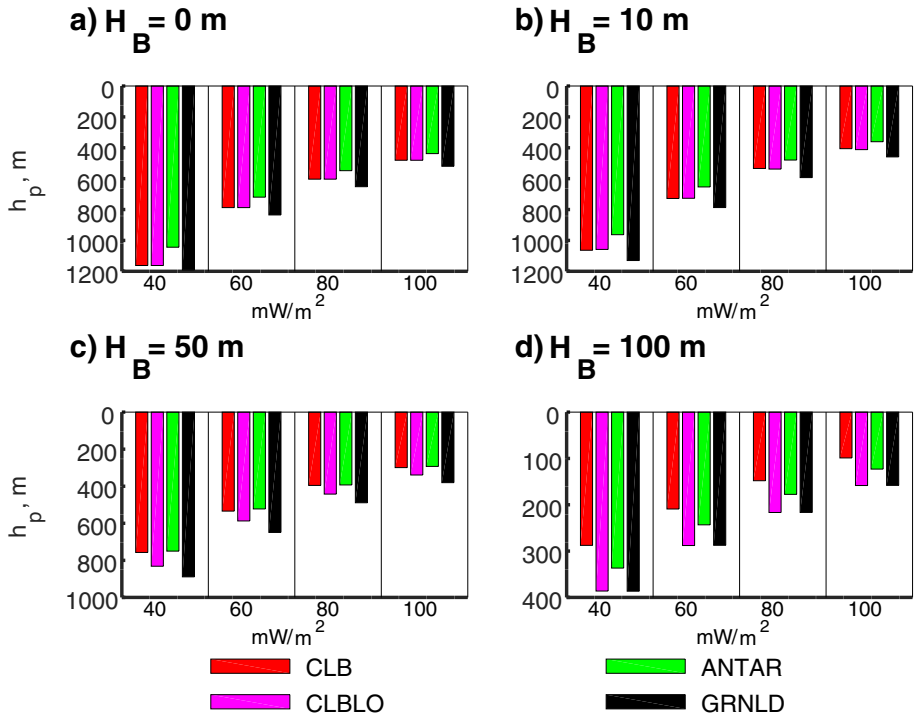

Fig. 6. Depth of the permafrost base below the seafloor averaged over the last millennium of the simulations with different values of the geothermal heat flux intensity G.

of R_D on G shows that this does not affect our qualitative results. Again, a transition between these cases occurs at $H_B = 50$ m, where $R_{h_b} \leq 11\%$ and $R_D \leq 16\%$ for the last 250 kyr and for the last 123 kyr if $G \leq 60$ Wm^{-2}, but, correspondingly, $R_{h_b} \geq 27\%$ and $R_D \geq 41\%$ if $G \geq 80$ Wm^{-2}. Nevertheless, all just listed values of the RMS uncertainty for h_b and D are smaller than their T_B counterparts. While no systematic dependence of absolute dependencies of both MHSZ base depth and MHSZ thickness on GHF is found, both R_{h_b} and R_D are positively correlated with G (Figs. 2, S2 and S3). This is again linked to the negative dependence of the forcing dataset–averaged h_b and D on geothermal heat flux intensity (see Fig. 8 as an example). No such dependence exists for R_{h_t}.

For all three MHSZ characteristics, the most pronounced differences between different forcing datasets are simulated for the deep shelf. For this shelf, we may summarise differences in the simulated MHSZ characteristics via fraction f_D of time when MHSZ exists in our simulation. For $G = 40$ mWm^{-2}, MHSZ is simulated for the whole last 250 kyr irrespective of T_B (Fig. 9). For other studied GHF values, f_D is smaller than unity and, as it was expected, decreases with increasing G. For the differences between different forcing datasets, the most marked differences of f_D are due to SL choice. For instance, in simulation CLB with $G = 60$ mWm^{-2} the fraction of time when MHSZ exists for $H_B = 100$ m is from 30 to 36% depending on time interval. For other simulations with the same value of G, but which utilise the foraminifera–derived SL, f_D is from 51 to 60% depending on forcing dataset and on time interval.

5.2. Apparent response time scales

Malakhova and Eliseev (2017) estimated apparent response time scales (ARTS) via time lags, τ_Y, between T_B and a variable of interest, Y. Such time lags were computed by finding the global maximum of cross–correlation function if positive correlation between T_B and Y is expected (for example, between the temperature of the upper boundary of the subsea sediments and temperature within the sediment column) and finding the global minimum of this function if such correlation is expected to be negative (for instance, when $Y = h_p$, h_b, D) (Ganopolski and Roche, 2009; Muryshev et al., 2017).

We note that the plateau in T_B, which is prescribed when the shelf is covered by water, may decrease thus calculated correlations. Taking this in mind, in the present paper we determined ARTS with SL in place of T_B. The respective plots with T_B as a base variable are shown in the Supplementary Information (Figs. S17 and S18). In brief, if we calculate our lags with respect to T_B rather than with respect to SL, the values are changed somewhat, their statistical significance is reduced.

Similar to that it was reported by Malakhova and Eliseev (2017), ARTS for temperature at depths $z > 500$ m are not robust numerically because of similarity of different maxima of the corresponding correlation functions. In addition, ARTS for MHSZ top depth is not robust numerically as well and their values are likely tied to change of the system between glacial and interglacial state. We acknowledge that this deserves a further study. In the present paper, we only present the results for those ARTS, which are relatively stable with respect to chosen time interval.

The determined ARTS is the most robust for permafrost base depth (Fig. 10). It is from 5.8 to 8.2 kyr for the coast and the shallow shelf (from 7.8 to 8.2 kyr if we discard simulation ANTAR) and is from 7.7 to 12 kyr for the intermediate and deep shelves. In general, calculated ARTS are not sensitive to G (cf. Figs. 10, S13, and S14 for τ_{h_p}; and Figs. 11, S15, and S16 for τ_D). As a whole, for all H_B values, the largest τ_{h_p} is obtained in simulation GRLND with the largest variations in forcing temperature. For the coast and for the shallow shelf, τ_{h_p} is smaller in simulation ANTAR (with the smallest variations of T_B among all employed here forcing datasets) in comparison to other simulations. For the intermediate and deep shelves, the smallest permafrost base ARTS is obtained for simulation CLB, which suggests an importance of sea level changes for permafrost response time scale for such shelf types. We note, however, that we are unable to conclude is it real dependencies on temperature and sea level or just a sampling variability. In any case, the permafrost base depth ARTS is constrained in our simulations to 20% for most cases except those for $H_B = 0$ for last 123 kyr (in this case, the uncertainty attains 36%) and for $H_B = 100$ m for last 250 kyr (relative

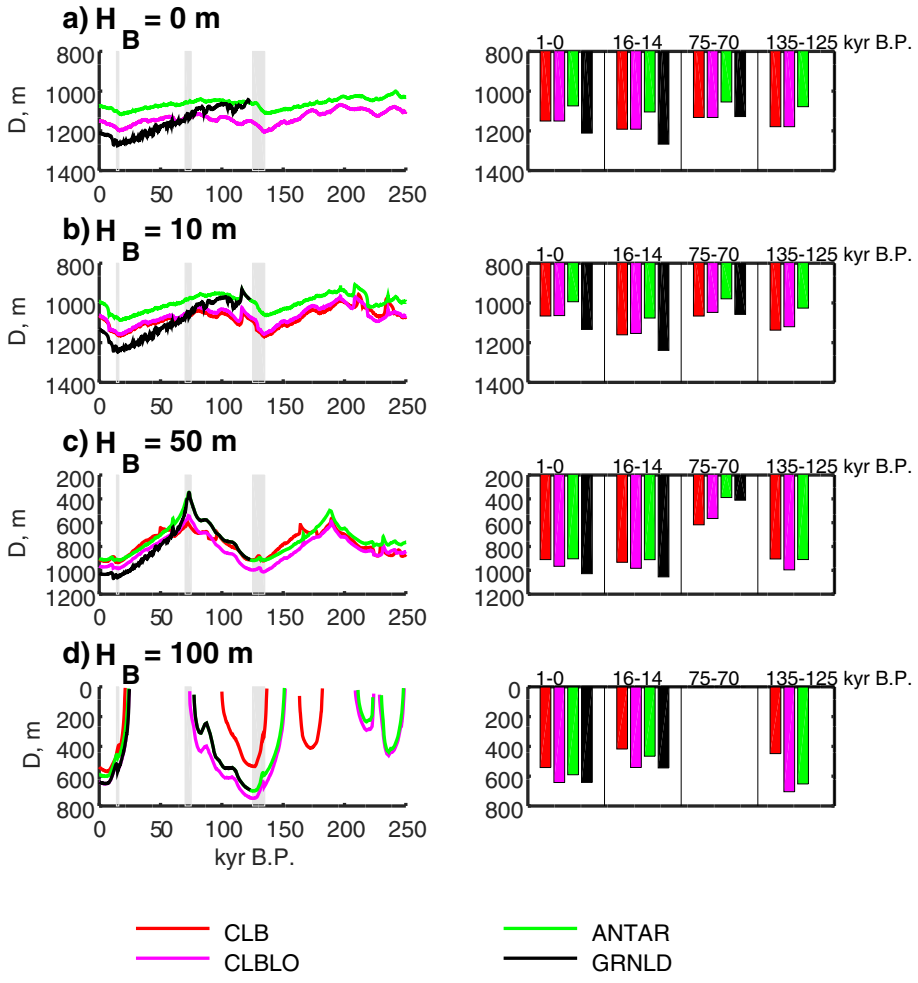

Fig. 7. Similar to Fig. 3 but for MHSZ thickness.

uncertainty is 28%).

Apparent response time scales for MHSZ thickness, τ_D, are relatively small for the coast and for the shallow shelf, from 1.9 to 6.9 kyr (from 1.9 to 5.4 kyr if one removes simulation GRNLD), and relatively large for the intermediate and deep shelves (from 8.4 to 15 kyr), see Figs. 11, S15, and S16. The respective values calculated with T_B in place of SL are generally similar, but are characterised by smaller statistical significance and smaller values for $H_B = 0$ m and 10 m (Fig. S5). The simulations with the foraminifera–derived SL to construct T_B lead to larger τ_D than those obtained in the CLB simulation except for the deep shelf. For the intermediate and deep shelves, τ_D differs no more than by 15% between different T_B. For the coast and the shallow shelf, the relative inter–simulation range is larger, with a two–fold difference between CLB and GRLND. In other respects, τ_D is insensitive to the choice of the forcing dataset.

6. Discussion and conclusions

We quantified the uncertainty in the simulation of the permafrost and an associated hydrate stability zone at the Arctic shelf, which is associated to the climate reconstructions uncertainty for the last 250 kyr. This was done by using the model for thermophysical processes in the subsea sediments. This model was forced by four time series of temperature at the sediment top, which were constructed by using different combinations of past surface air temperature and past sea level. These combinations partly come from the proxy data for the last 400 kyr and partly simulated by an Earth system model. Thus constructed forcings are chosen to cover wide possibilities of past climate changes rather than to represent precise history of the east Eurasian Arctic shelf. In particular, temperature deviations for the last Glacial Maximum from the present–day state differ by a factor of 2 between these series.

We use the ratio r between the intra–ensemble range and the ensemble mean of a given variable to quantify uncertainty arising from uncertainty in our forcing datasets. To quantify the uncertainty representative for a given time interval, we use the root–mean–square value of r. Our estimates are conservative because they likely overestimate true uncertainty.

Despite the marked differences between our forcing datasets (RMS uncertainty for the last 250 kyr is equal to 39% for SL and to 79% for T_a, we are able to constrain the responses of the studied variables to changes of T_B in the Pleistocene for the coast and for the shallow and intermediate–depth shelves. In these cases, this bound for permafrost base depth and for hydrate stability zone characteristics (depth of its bottom boundary and its thickness) is $\leq 45\%$ provided that the geothermal heat flux intensity is not larger than 80 $\mathrm{mW\,m^{-2}}$ except during relatively isolated time intervals.

However, for the deep shelf, which is flooded for about 90% of our simulation time (Table S2; note for comparison that the corresponding value for the intermediate–depth shelf is around one half), different forcing time series may even lead to qualitatively different behaviour of the sediment thermophysical characteristics. The most prominent example of the latter is the time interval around 170 kyr B.P., when one forcing (CLB) results in formation of a rather deep frozen layer in the sediments and formation of MHSZ for about 20 kyr, while in simulations with other forcings this event is missed. The same CLB forcing

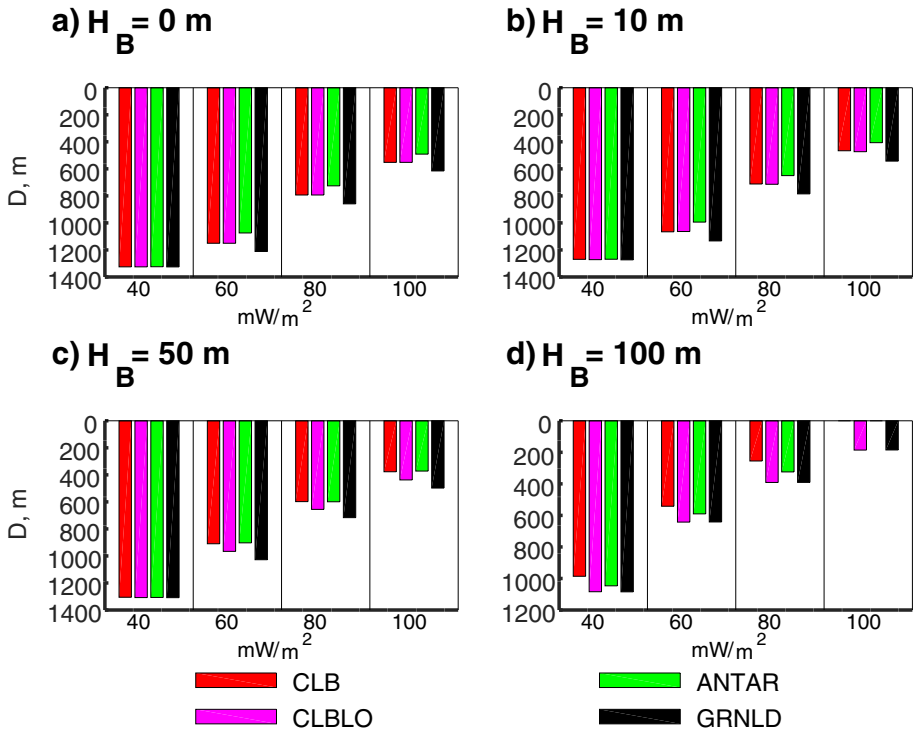

Fig. 8. Thickness of the methane hydrates stability zone averaged over the last millennium of the simulations with different values of the geothermal heat flux intensity *G*.

dataset is also characterised by the smallest fraction of time when MHSZ exists in the deep shelf (Fig. 9). This dataset differs from other forcings by prescribed sea level. Thus, details of the prescribed sea level changes play a crucial role in uncertainty of the simulated subsea permafrost and MHSZ in the deep shelf sediments. This is basically due to high sensitivity of the length of the time interval when deep shelf is above the sea level.

In some cases, systematic dependencies of RMS uncertainties of MHSZ characteristics on geothermal heat flux are found.

We also studied the dependence of the apparent response time

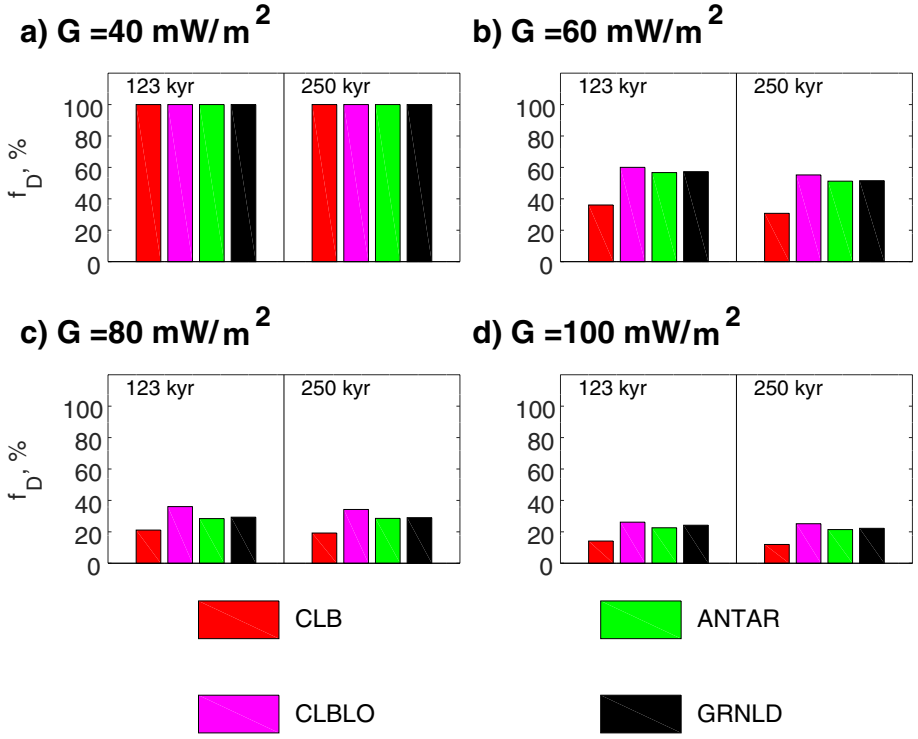

Fig. 9. Fraction of time when hydrate stability zone exists for shelf with contemporary depth 100 m in simulations with different geothermal heat flux intensity *G* (abscissae).

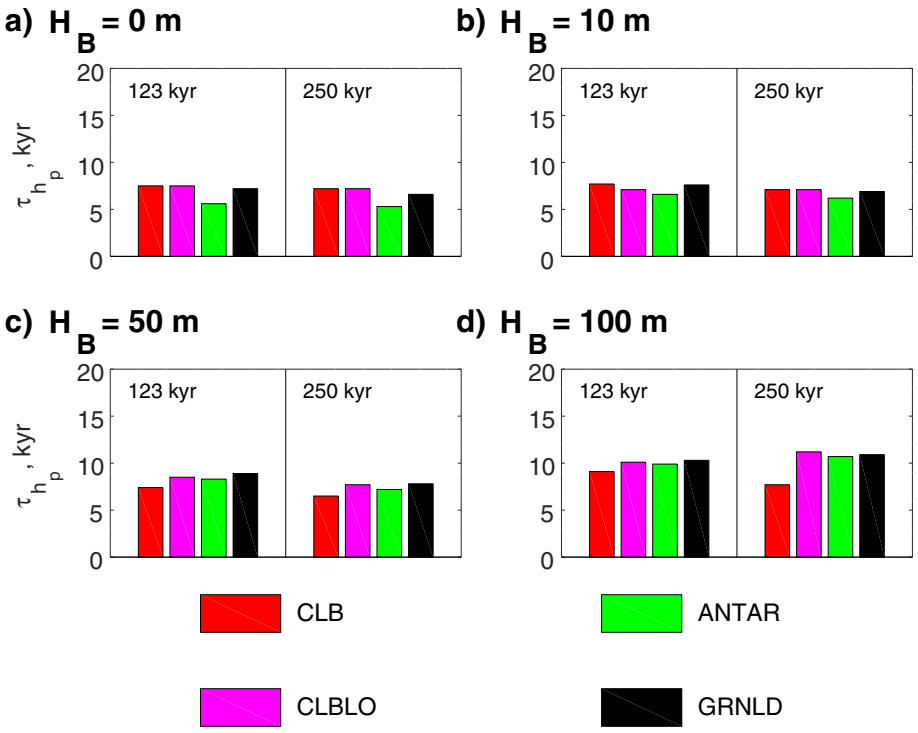

Fig. 10. Apparent response time scales of the subsea permafrost base depth to sea level changes in simulations with $G = 80\,\mathrm{mW\,m^{-2}}$.

scales on forcing uncertainty. As a whole, the ARTS values for permafrost base depth and hydrate stability zone thickness are constrained in our simulations to 20% for most cases. In principle, apparent response time scales reflect characteristic time of signal propagation in the sediments and, thus, are expected to be independent on forcing amplitude. However, such reasoning is strictly valid only for linear problem, while the heat propagation in a media is nonlinear provided that phase transitions are important. Some hints for ARTS dependence on amplitude of the forcing are found in our simulations, but we can not consistently distinguish it from the sampling variability. Nonetheless, we could support the conclusion made by Malakhova and Eliseev (2017) that the permafrost base depth and hydrate stability zone thickness ARTS are at least several kiloyears. Therefore, the observed methane release can not be related to the climate warming occurred during last decades as it is claimed in (Shakhova et al., 2015) but likely is a response to multimillennium–scale climate changes (Dmitrenko

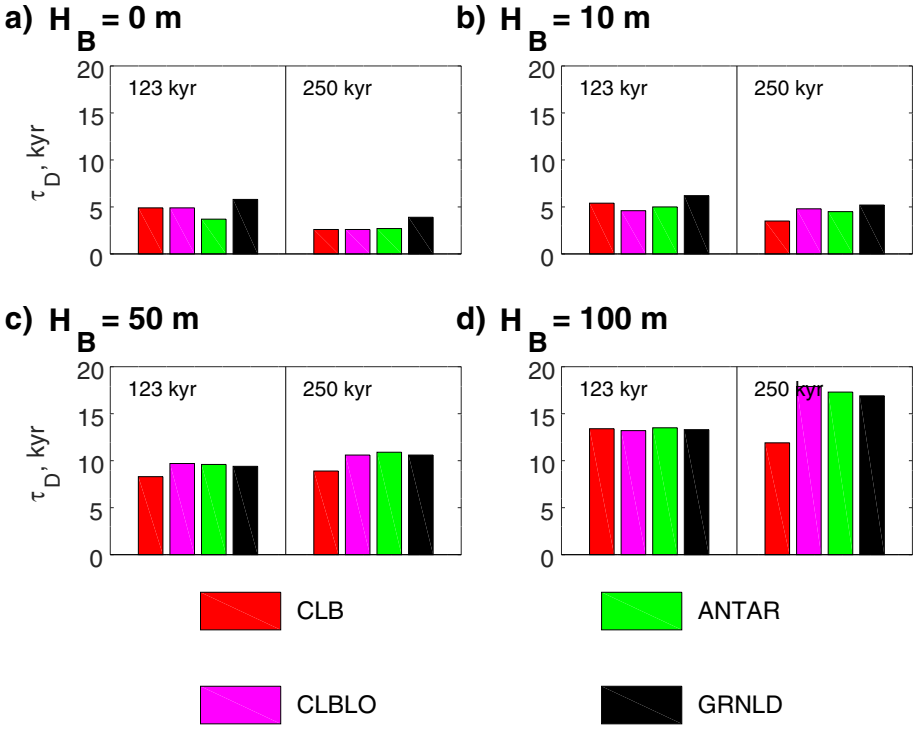

Fig. 11. Apparent response time scales of methane hydrate stability zone thickness to sea level changes in simulations with $G = 80\,\mathrm{mW\,m^{-2}}$.

et al., 2011; Anisimov et al., 2014; Malakhova and Eliseev, 2017). In addition, ARTS are not sensitive to GHF. This again is somewhat expected because they reflect internal dynamics rather than imposed boundary conditions.

We found no systematic dependence of our results on accounting for millennium–scale temperature variability. This is consistent with the estimated ARTS, which are larger than the millennium timescale. This reduces requirements for time resolution of forcing datasests for the problem at hand: time series resolving kiloyear time scales are sufficient for simulating thermophysical state of the subsea sediments.

Our paper has a number of potentially important limitations.

At first, our T_B implementation assumes that, for a given H_B, the flooded shelf always experiences the same temperature. This is likely unrealistic when water layer above the sediments is thin. We note in this respect that there are rather long (up to 2 kyr) time intervals when shelf is covered by water layer with thickness ≤ 2 m. Such water layers may be heated down to the bottom in summer and may freeze in winter. Thus, a smooth change of T_B is expected during shelf flooding and opening rather than a temperature jump as prescribed in our implementation. This might affect behaviour of the subsea permafrost and associated MHSZ. In particular, one of such time intervals is around 170 kyr B.P., when qualitative simulation differences between different forcing datasets are found. Such difference may be caused by the overestimated sensitivity of T_B to recent shelf flooding or shortly upcoming shelf exposition.

This issue is additionally complicated by millennium–scale sea changes which are possible during interglacials (Kopp et al., 2013). This issue is different from that related to temperature variability with similar timescale (see above) because if sea level fluctuates around specific value of H_B, it also able to produce high–frequency temperature jumps which are set by the difference between annual mean surface air temperature during shelf exposure and the prescribed near–bottom oceanic temperature during oceanic transgressions. Millennium–scale SL variations are neither resolved by the foraminifera–derived sea level reconstruction (Waelbroeck et al., 2002) nor simulated by Climber–2. However, because typical magnitude of these variations is of similar order of magnitude to variations exhibited by the NGRIP reconstructions, it is expected to be unimportant for our purposes.

Nevertheless, we performed additional simulations, in which

$$T_B = w(H_B, SL)T_{B,f} + (1 - w(H_B, SL))T_{B,e}. \quad (3)$$

Here $w(H_B, SL)$ is weight dependent on contemporary shelf depths and time-varying sea level. If shelf is exposed ($SL < -H_B$), this weights is set equal to zero. If shelf is covered by water, and the water layer thickness is above 5 m, $w(H_B, SL) = 1$. If the water layer thickness is between 0 and 5 m, the weight is set equal to $(SL + H_B)/5$ m. Thus calculated T_B is a smoothed version of the sediment top temperature specification outlined in Sect. 3. We found no discernible differences between our main simulations and these additional simulations neither for simulated thermophysical variables except during isolated time intervals nor for the estimated ARTS. Therefore, we conclude that millennium–scale variability both in reconstructed surface air temperatures and in sea level is immaterial for major conclusions of our paper.

Besides, we prescribe the freezing temperature of the oceanic water as $T_F = -1°C$. Another choices of values for these variables are possible. For example, Romanovskii et al. (2005) used $T_F = -2°C$. Moreover, T_F depends on salinity and on pressure, therefore, on H_B and on the phase of the glaciation/deglaciation (Razumov et al., 2014; Anisimov et al., 2012). However, substantial modification of T_F owing to such effects was found only for shallow shelf, while for the intermediate and deep shelf it is of minor importance. While the precise choice of these values may affect our results qualitatevely, it is unlikely that it is of major importance for the results reported here because only the difference $T_F - T_B$ is material for our simulations. Uncertainty due to the choice of the latter difference, in turn, is partly (albeit far from completely) accounted in uncertainty of datings of shelf exposure and flooding. In addition, for any reasonable choice of T_F and T_B, this difference is not larger than few Kelvins when shelf is covered by water. This magnitude is much smaller than magnitude of jumps imposed by our implementation of T_B.

Further, we neglected possible formation of thermokarst lakes during glacial terminations at a still exposed shelf owing to permafrost thaw. Such lakes set the values T_B slightly above 0°C (Moridis, 2003; Burn, 2002). This speeds up the permafrost thaw and could lead to formation of perforating taliks (Malakhova and Eliseev, 2018). Similar taliks may occur in the rift zones where heat flow from the Earth interior is around 100 $mW\,m^{-2}$. Thermokarst lakes formation is neglected in the present paper because it is unclear how to prescribe their formation and subsequent draining at different stages of glaciations/deglaciations. Impact of enhanced heat flow in the rift zones, in turn, was partly studied by Malakhova and Eliseev (2018). We acknowledge that implementation of these effects could change our results even qualitatively.

In addition, we neglect phase transitions of methane hydrates in the model. Latent heat of fusion for methane hydrates is 28% larger than for pure water (Rueff et al., 1988). Implementing this into the model would increase ARTS for thermophysical properties in the sediment. Such enhanced inertia is expected to suppress the sensitivity of the changes to details of the imposed forcing, on one hand. On the other, it would increase nonlinearity of the heat propagation in the sediments, thus making the response more sensitive to such details.

Finally, we set pore water salinity equal to zero in the equilibrium pressure–temperature equations for methane hydrates. This likely enhances stability of methane hydrates because they have higher temperature triple point in fresh than in salty water (Buffett, 2000). For reasonable values of governing parameters, the typical triple point depression is about from 1 to 2°C, which is much smaller than the simulated variations of T_B at the sediment top (Fig. 1) but somewhat comparable to the respective variations of temperature at larger depths (Figs. 3, S5–S7). We also made additional calculations with an explicit implementation of the water pore salinity in this equation and the prescribed salinity value of 20 psu. This resulted in the vertical shift of MHSZ by about several tens of meters. In other respects, the results of these simulations are very similar to those reported above. We highlight that water pore salinity is taken into account in the negative value of T_B. More elaborated treatment of salinity needs an explicit scheme for salt transport in the sediments. Despite of the results of our additional simulations, at the date, we can not exclude possibility that our neglect of salinity influence on methane hydrate stability zone boundaries may affect our quantitative results.

Declaration of Competing Interest

The authors declare that they have no known competing financial interests or personal relationships that could have appeared to influence the work reported in this paper.

Acknowledgements

Authors are grateful to the anonymous reviewer whose comments greatly improved presentation of results. Our work has been supported by the Russian Foundation for Basic Research (projects 17–05–00396, 18–05–00087, 18–05–60,111, and 19–05–00409). It was also funded by the government program for federal support of Kazan (Volga region) Federal University for enhancing its competitiveness among the worlds leading scientific and educational centers A.V.E. contribution was partly supported by the Lomonosov Moscow State University project no. 01200408543. V.V.M. contribution was partly supported by the ICMMG project 0315-2019-0004.

Appendix A. Supplementary data

Supplementary data to this article can be found online at https://doi.org/10.1016/j.gloplacha.2020.103249.

References

Anisimov, O., Borzenkova, I., Lavrov, S., Strel'chenko, Y., 2012. The current dynamics of the submarine permafrost and methane emissions on the shelf of the Eastern Arctic seas. Ice Snow 52, 97–105 (in Russian).

Anisimov, O., Zaboikina, Y., Kokorev, V., Yurganov, L., 2014. Possible causes of methane release from the East Arctic seas shelf. Ice Snow 54, 69–81 (in Russian).

Annan, J., Hargreaves, J., 2013. A new global reconstruction of temperature changes at the last Glacial maximum. Clim. Past 9, 367–376. https://doi.org/10.5194/cp-9-367-2013.

Bartlein, P., Harrison, S., Brewer, S., Connor, S., Davis, B., Gajewski, K., Guiot, J., Harrison-Prentice, T., Henderson, A., Peyron, O., Prentice, I., Scholze, M., Seppa, H., Shuman, B., Sugita, S., Thompson, R., Viau, A., Williams, J., Wu, H., 2011. Pollen–based continental climate reconstructions at 6 and 21 ka: a global synthesis. Clim. Dyn. 37, 775–802. https://doi.org/10.1007/s00382-010-0904-1.

Bauch, H., Mueller-Lupp, T., Taldenkova, E., Spielhagen, R., Kassens, H., Grootes, P., Thiede, J., Heinemeier, J., Petryashov, V., 2001. Chronology of the Holocene transgression at the North Siberian margin. Glob. Planet. Chang. 31, 125–139. https://doi.org/10.1016/S0921-8181(01)00116-3.

Buffett, B., 2000. Clathrate hydrates. Annu. Rev. Earth Planet. Sci. 28, 477–507. https://doi.org/10.1146/annurev.earth.28.1.477.

Burn, C., 2002. Tundra lakes and permafrost, Richards Island, western Arctic coast, Canada. Can. J. Earth Sci. 39, 1281–1298. https://doi.org/10.1139/e02-035.

Davies, J., 2013. Global map of solid Earth surface heat flow. Geochem. Geophys. Geosyst. 14, 4608–4622. https://doi.org/10.1002/ggge.20271.

Denisov, S., Arzhanov, M., Eliseev, A., Mokhov, I., 2011. Assessment of the response of subaqueous methane hydrate deposits to possible climate change in the twenty first century. Dokl. Earth Sci. 441, 1706–1709. https://doi.org/10.1134/S1028334X11120129.

Dmitrenko, I., Kirillov, S., Tremblay, L., Kassens, H., Anisimov, O., Lavrov, S., Razumov, S., Grigoriev, M., 2011. Recent changes in shelf hydrography in the Siberian Arctic: potential for subsea permafrost instability. J. Geophys. Res.: Oceans 116https://doi.org/10.1029/2011JC007218. C10027.

Dutton, A., Lambeck, K., 2012. Ice volume and sea level during the last interglacial. Science 337, 216–219. https://doi.org/10.1126/science.1205749.

Eliseev, A., Malakhova, V., Arzhanov, M., Golubeva, E., Denisov, S., Mokhov, I., 2015. Changes in the boundaries of the permafrost layer and the methane hydrate stability zone on the Eurasian Arctic Shelf, 1950–2100. Dokl. Earth Sci. 465, 1283–1288. https://doi.org/10.1134/S1028334X15120107.

EPICA Community Members, 2004. Eight glacial cycles from an Antarctic ice core. Nature 429, 623–628. https://doi.org/10.1038/nature02599.

Ganopolski, A., Calov, R., 2011. The role of orbital forcing, carbon dioxide and regolith in 100 kyr glacial cycles. Clim. Past 7, 1415–1425. https://doi.org/10.5194/cp-7-1415-2011.

Ganopolski, A., Roche, D., 2009. On the nature of lead–lag relationships during glacial–interglacial climate transitions. Quat. Sci. Rev. 28https://doi.org/10.1016/j.quascirev.2009.09.019. 3361–337.

Hunter, S., Goldobin, D., Haywood, A., Ridgwell, A., Rees, J., 2013. Sensitivity of the global submarine hydrate inventory to scenarios of future climate change. Earth Planet. Sci. Lett. 367, 105–115. https://doi.org/10.1016/j.epsl.2013.02.017.

Kindler, P., Guillevic, M., Baumgartner, M., Schwander, J., Landais, A., Leuenberger, M., 2014. Temperature reconstruction from 10 to 120 kyr b2k from the NGRIP ice core. Clim. Past 10, 887–902. https://doi.org/10.5194/cp-10-887-2014.

Kopp, R., Simons, F., Mitrovica, J., Maloof, A., Oppenheimer, M., 2009. Probabilistic assessment of sea level during the last interglacial stage. Nature 462, 863–867. https://doi.org/10.1038/nature08686.

Kopp, R., Simons, F., Mitrovica, J., Maloof, A., Oppenheimer, M., 2013. A probabilistic assessment of sea level variations within the last interglacial stage. Geophys. J. Int. 193, 711–716. https://doi.org/10.1093/gji/ggt029.

MacDonald, G., 1990. Role of methane clathrates in past and future climates. Clim. Chang. 16, 247–281. https://doi.org/10.1007/BF00144504.

Malakhova, V., 2016. On the thermal influence of thermokarst lakes on the subsea permafrost evolution. Proc. SPIE 10035https://doi.org/10.1117/12.2248714. 100355U.

Malakhova, V., Eliseev, A., 2017. The role of heat transfer time scale in the evolution of the subsea permafrost and associated methane hydrates stability zone during glacial cycles. Glob. Planet. Chang. 157, 18–25. https://doi.org/10.1016/j.gloplacha.2017.08.007.

Malakhova, V., Eliseev, A., 2018. Influence of rift zones and thermokarst lakes on the formation of subaqueous permafrost and the stability zone of methane hydrates of the Laptev Sea shelf in the Pleistocene. Ice Snow 58, 231–242. https://doi.org/10.15356/2076-6734-2018-2-231-242. (in Russian).

Malakhova, V., Golubeva, E., 2016. Estimation of the permafrost stability on the East Arctic shelf under the extreme climate warming scenario for the XXI century. Ice Snow 56, 61–72. https://doi.org/10.15356/2076-6734-2016-1. (in Russian).

MARGO Project Members, 2009. Constraints on the magnitude and patterns of ocean cooling at the last Glacial maximum. Nat. Geosci. 2, 127–132. https://doi.org/10.1038/ngeo411.

Masson-Delmotte, V., Schulz, M., Abe-Ouchi, A., Beer, J., Ganopolski, A., González Rouco, J., Jansen, E., Lambeck, K., Luterbacher, J., Naish, T., Osborn, T., Otto-Bliesner, B., Quinn, T., Ramesh, R., Rojas, M., Shao, X., Timmermann, A., 2013. Information from paleoclimate archives. In: Stocker, T., Qin, D., Plattner, G.K., Tignor, M., Allen, S., Boschung, J. ... Midgley, P. (Eds.), Climate Change 2013: The Physical Science Basis. Contribution of Working Group I to the Fifth Assessment Report of the Intergovernmental Panel on Climate Change. Cambridge University Press, Cambridge and New York, pp. 383–464.

McKay, N., Overpeck, J., Otto-Bliesner, B., 2011. The role of ocean thermal expansion in last Interglacial Sea level rise. Geophys. Res. Lett. 38https://doi.org/10.1029/2011GL048280. L14605.

Montoya, M., von Storch, H., Crowley, T., 2000. Climate simulation for 125 kyr BP with a coupled ocean–atmosphere general circulation model. J. Clim. 13, 1057–1072. https://doi.org/10.1175/1520-0442(2000)013<1057:CSFKBW>2.0.CO;2.

Moridis, G., 2003. Numerical studies of gas production from methane hydrates. Soc. Petrol. Eng. J. 32, 359–370. https://doi.org/10.2118/87330-PA.

Muryshev, K., Eliseev, A., Mokhov, I., Timazhev, A., 2017. Lead–lag relationships between global mean temperature and the atmospheric CO_2 content in dependence of the type and time scale of the forcing. Glob. Planet. Chang. 148, 29–41. https://doi.org/10.1016/j.gloplacha.2016.11.005.

Nicolsky, D., Romanovsky, V., Romanovskii, N., Kholodov, A., Shakhova, N., Semiletov, I., 2012. Modeling sub–sea permafrost in the East Siberian Arctic Shelf: the Laptev Sea region. J. Geophys. Res. Earth Surf. 117https://doi.org/10.1029/2012JF002358. F03028.

O'Connor, F., Boucher, O., Gedney, N., Jones, C., Folberth, G., Coppell, R., Friedlingstein, P., Collins, W., Chappellaz, J., Ridley, J., Johnson, C., 2010. Possible role of wetlands, permafrost, and methane hydrates in the methane cycle under future climate change: a review. Rev. Geophys. 48https://doi.org/10.1029/2010RG000326. RG4005.

Otto-Bliesner, B., Rosenbloom, N., Stone, E., McKay, N., Lunt, D., Brady, E., Overpeck, J., 2013. How warm was the last interglacial? New mode—data comparisons. Philos. Trans. R. Soc. Ser. A 371, 20130097. https://doi.org/10.1098/rsta.2013.0097.

Overduin, P., Schneider von Deimling, T., Miesner, F., Grigoriev, M., Ruppel, C., Vasiliev, A., Lantuit, H., Juhls, B., Westermann, S., 2019. Submarine permafrost map in the arctic modeled using 1–D transient heat flux (SuPerMAP). J. Geophys. Res.: Oceans 124, 3490–3507. https://doi.org/10.1029/2018JC014675.

Past Interglacials Working Group of PAGES, 2016. Interglacials of the last 800,000 years. Rev. Geophys. 54, 162–219. https://doi.org/10.1002/2015RG000482.

Petrenko, V., Smith, A., Schaefer, H., Riedel, K., Brook, E., Baggenstos, D., Harth, C., Hua, Q., Buizert, C., Schilt, A., Fain, X., Mitchell, L., Bauska, T., Orsi, A., Weiss, R., Severinghaus, J., 2017. Minimal geological methane emissions during the Younger Dryas–Preboreal abrupt warming event. Nature 548, 443–446. https://doi.org/10.1038/nature23316.

Pollack, H., Hurter, S., Johnson, J., 1993. Heat flow from the Earth's interior: analysis of the global data set. Rev. Geophys. 31, 267–280. https://doi.org/10.1029/93RG01249.

Portnov, A., Mienert, J., Serov, P., 2014. Modeling the evolution of climate–sensitive Arctic subsea permafrost in regions of extensive gas expulsion at the West Yamal shelf. J. Geophys. Res. Biogeosci. 119, 2082–2094. https://doi.org/10.1002/2014JG002685.

Razumov, S., Spektor, V., Grigoriev, M., 2014. Model of the post–Cenozoic evolution of the cryolithozone of the shelf of the western part of the Laptev Sea. Oceanology 54, 637–649. https://doi.org/10.1134/S0001437014040092.

Reagan, M., Moridis, G., 2008. Dynamic response of oceanic hydrate deposits to ocean temperature change. J. Geophys. Res.: Oceans 113https://doi.org/10.1029/2008JC004938. C12023.

Romanovskii, N., Hubberten, H.W., Gavrilov, A., Eliseeva, A., Tipenko, G., 2005. Offshore permafrost and gas hydrate stability zone on the shelf of East Siberian Seas. Geo-Mar. Lett. 25, 167–182. https://doi.org/10.1007/s00367-004-0198-6.

Rueff, R., Dendy Sloan, E., Yesavage, V., 1988. Heat capacity and heat of dissociation of methane hydrates. AICHE J. 34, 1468–1576. https://doi.org/10.1002/aic.690340908.

Schmittner, A., Saenko, O., Weaver, A., 2003. Coupling of the hemispheres in observations and simulations of glacial climate change. Quat. Sci. Rev. 22, 659–671. https://doi.org/10.1016/S0277-3791(02)00184-1.

Sclater, J., Christie, P., 1980. Continental stretching: an explanation of the Post–Mid–cretaceous subsidence of the Central North Sea Basin. J. Geophys. Res. Solid Earth 85, 3711–3739. https://doi.org/10.1029/JB085iB07p03711.

Shakhova, N., Semiletov, I., Sergienko, V., Lobkovsky, L., Yusupov, V., Salyuk, A., Salomatin, A., Chernykh, D., Kosmach, D., Panteleev, G., Nicolsky, D., Samarkin, V., Joye, S., Charkin, A., Dudarev, O., Meluzov, A., Gustafsson, O., 2015. The East Siberian Arctic Shelf: towards further assessment of permafrost–related methane fluxes and role of sea ice. Philos. Trans. R. Soc. Ser. A 373, 20140451. https://doi.org/10.1098/rsta.2014.0451.

Shakun, J., Clark, P., He, F., Marcott, S., Mix, A., Liu, Z., Otto-Bliesner, B., Schmittner, A., Bard, E., 2012. Global warming preceded by increasing carbon dioxide concentrations during the last deglaciation. Nature 484, 49–54. https://doi.org/10.1038/nature10915.

Sowers, T., 2006. Late quaternary atmospheric CH_4 isotope record suggests marine clathrates are stable. Science 311, 838–840. https://doi.org/10.1126/science.1121235.

Stirling, C., Esat, T., Lambeck, K., McCulloch, M., 1998. Timing and duration of the last Interglacial: evidence for a restricted interval of widespread coral reef growth. Earth Planet. Sci. Lett. 160, 745–762. https://doi.org/10.1016/S0012-821X(98)00125-3.

Stocker, T., Johnsen, S., 2003. A minimum thermodynamic model for the bipolar seesaw. Paleoceanography 18, 1087. https://doi.org/10.1029/2003PA000920.

Thompson, W., Goldstein, S., 2005. Open–system coral ages reveal persistent suborbital sea–level cycles. Science 308, 401–404. https://doi.org/10.1126/science.1104035.

Turney, C., Jones, R., 2010. Does the Agulhas current amplify global temperatures during super–interglacials? J. Quart. Sci. 25, 839–843. https://doi.org/10.1002/jqs.1423.

Waelbroeck, C., Labeyrie, L., Michel, E., Duplessy, J., McManus, J., Lambeck, K., Balbon, E., Labracherie, M., 2002. Sea–level and deep water temperature changes derived from benthic foraminifera isotopic records. Quat. Sci. Rev. 21, 295–305. https://doi.org/10.1016/S0277-3791(01)00101-9.

Supplementary information to

Uncertainty in temperature and sea level datasets for the Pleistocene glacial cycles: implications for thermal state of the subsea sediments

Valentina V. Malakhova and Alexey V. Eliseev

Table S1. Correlation coefficients between different datasets for sea level (SL) and temperature (T) employed in the present paper

dataset pair	0–123 kyr B.P.	0–250 kyr B.P.
SL (Waelbroeck et al., 2002)–SL Climber	0.93	0.87
T Climber–T EPICA	0.81	0.79
T Climber–T NGRIP	0.71	
T EPICA–T NGRIP	0.79	
SL (Waelbroeck et al., 2002)–T Climber	0.88	0.85
SL (Waelbroeck et al., 2002)–T EPICA	0.81	0.80
SL (Waelbroeck et al., 2002)–T NGRIP	0.70	
SL Climber–T Climber	0.94	0.92
SL Climber–T EPICA	0.81	0.74
SL Climber–T NGRIP	0.68	

Table S2. Fraction of time (per cent) when shelf is covered by water for two employed sea level reconstructions and for different contemporary shelf depths H_B

H_B	(Waelbroeck et al., 2002)		Climber	
	0–123 kyr B.P.	0–250 kyr B.P.	0–123 kyr B.P.	0–250 kyr B.P.
0	0	0	0	0
10 m	9	11	12	12
50 m	49	46	55	56
100 m	90	86	94	93

Table S3. Values of sea level (m) for two employed reconstructions averaged over specified time intervals

dataset	20–18 kyr B.P.	50–40 kyr B.P.	130–120 kyr B.P.	150–145 kyr B.P.	175–165 kyr B.P.
(Waelbroeck et al., 2002)	-121	-55	+2	-112	-74
Climber	-109	-72	-3	-57	-26

Table S4. Surface air temperature (°C) for different datasets employed in the present paper averaged over specified time intervals. For all three sources, the present–day temperature is assumed to be equal to −12°C.

dataset	20–18 kyr B.P.	55–45 kyr B.P.	75–70 kyr B.P.
Climber	-27.4	-18.7	-20.1
EPICA	-19.9	-18.3	-18.2
NGRIP	-25.3	-21.0	-26.5

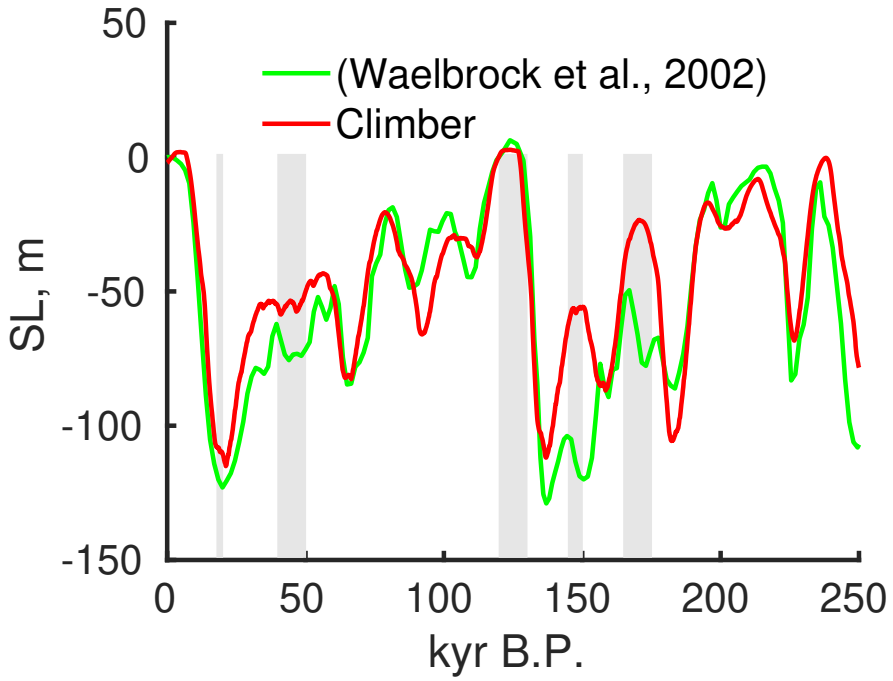

Fig. S1. Sea level changes for two employed reconstructions. Gray rectangles depict time intervals which were used to calculate the statistics in Table S3.

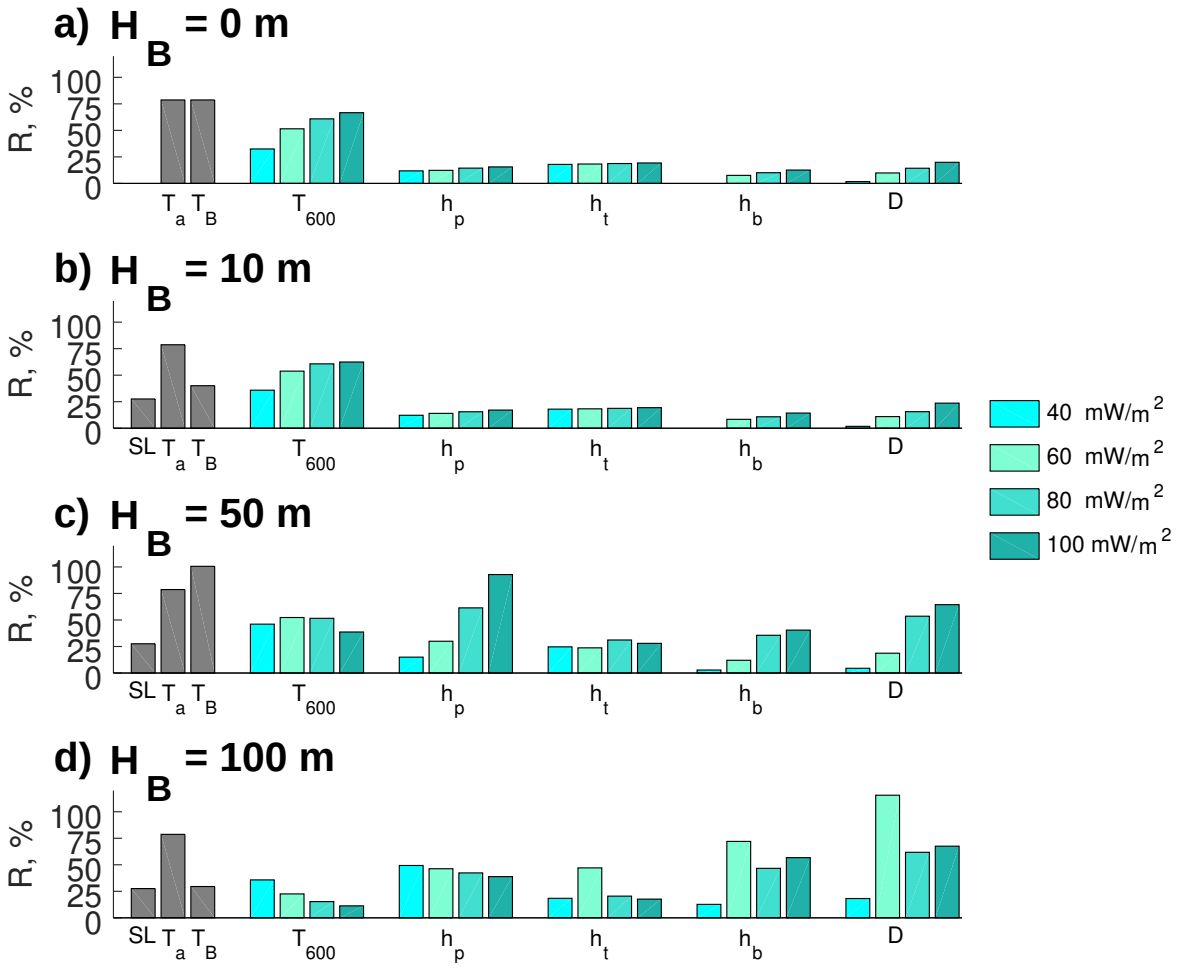

Fig. S2. Similar to Fig. 2 of the main text, but for the last 123 kyr.

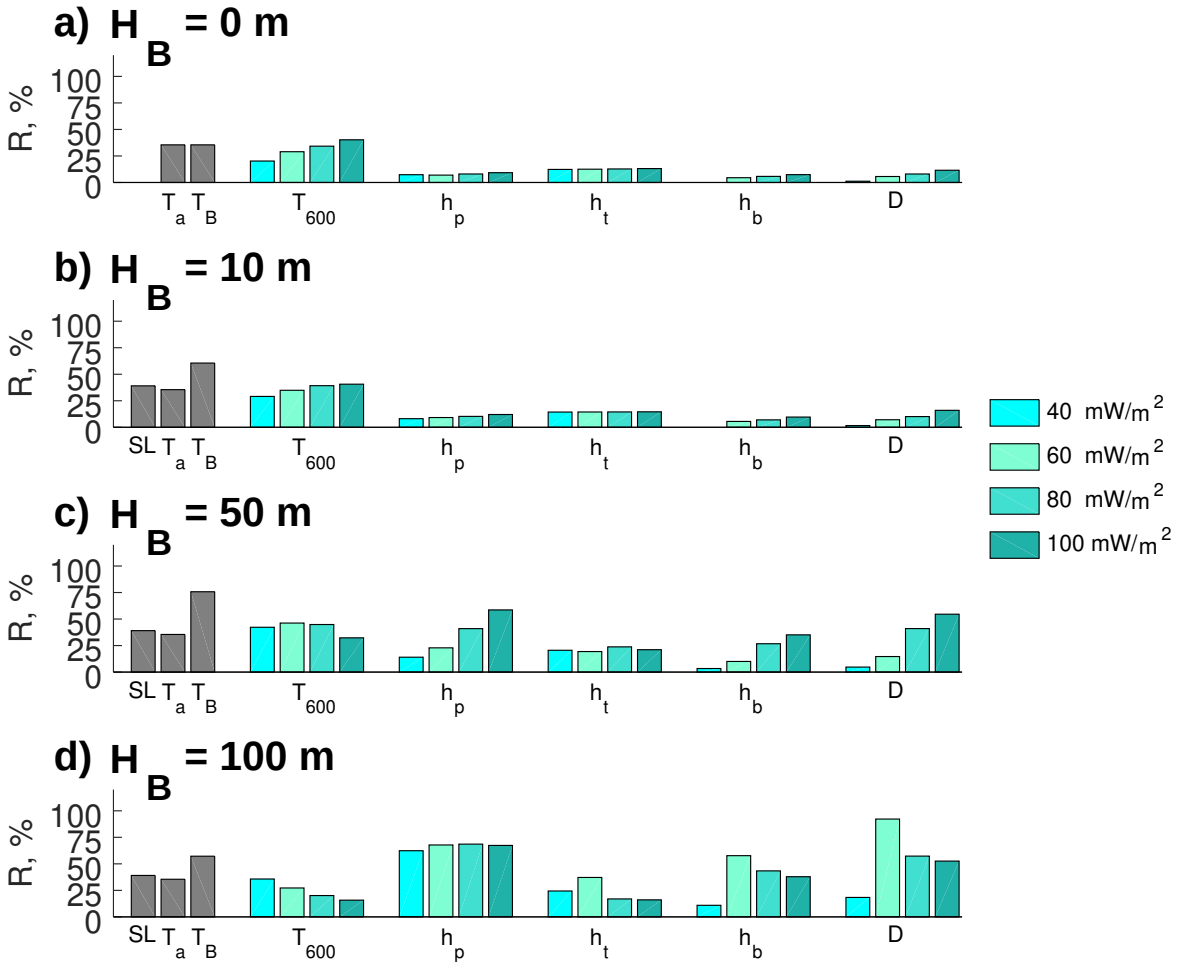

Fig. S3. Similar to Fig. 2 of the main text, but discarding simulation ANTAR in calculation of r.

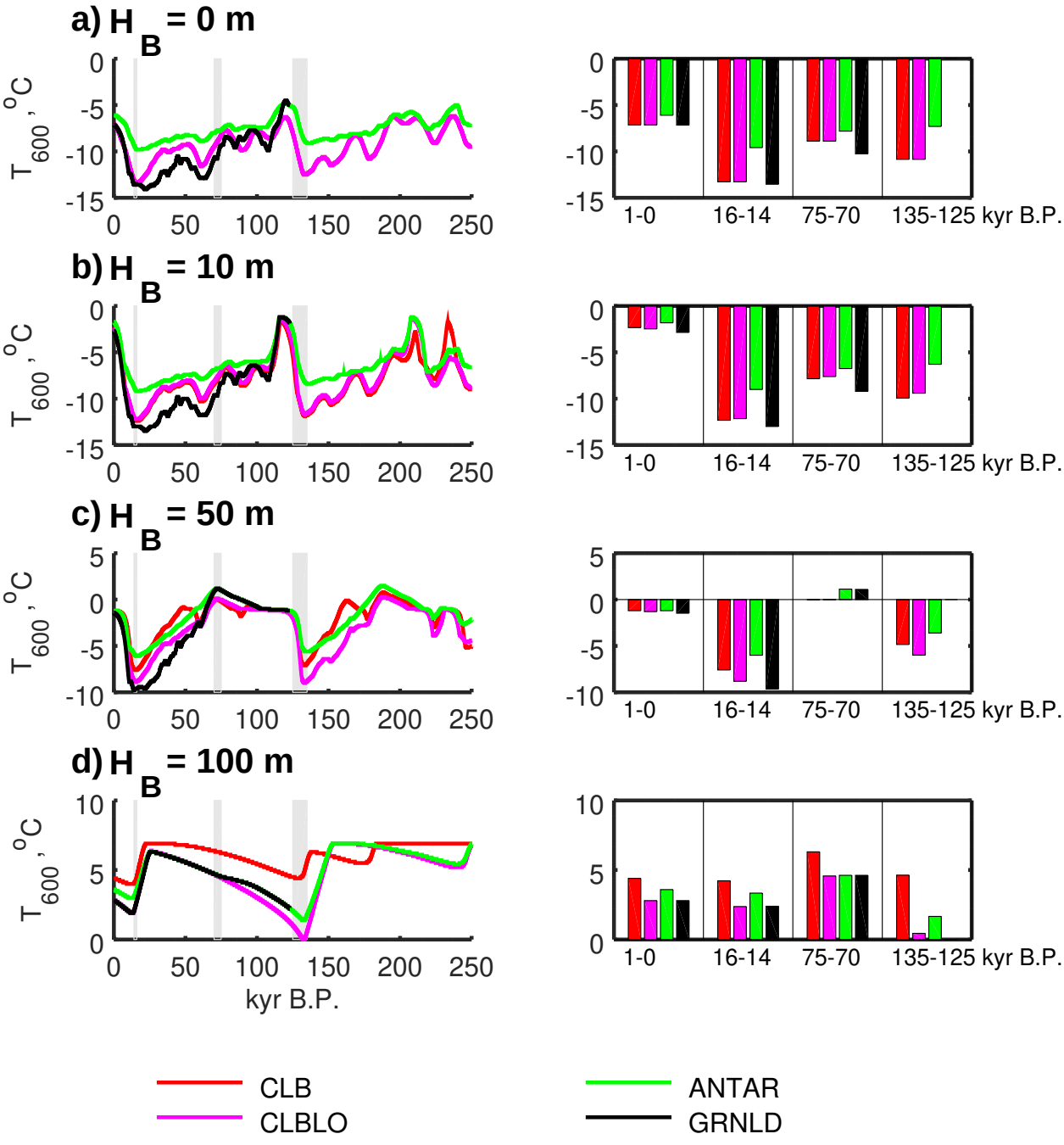

Fig. S4. Similar to Fig. 3 of the main text, but for the simulations with $G = 40\,\mathrm{mW\,m^{-2}}$.

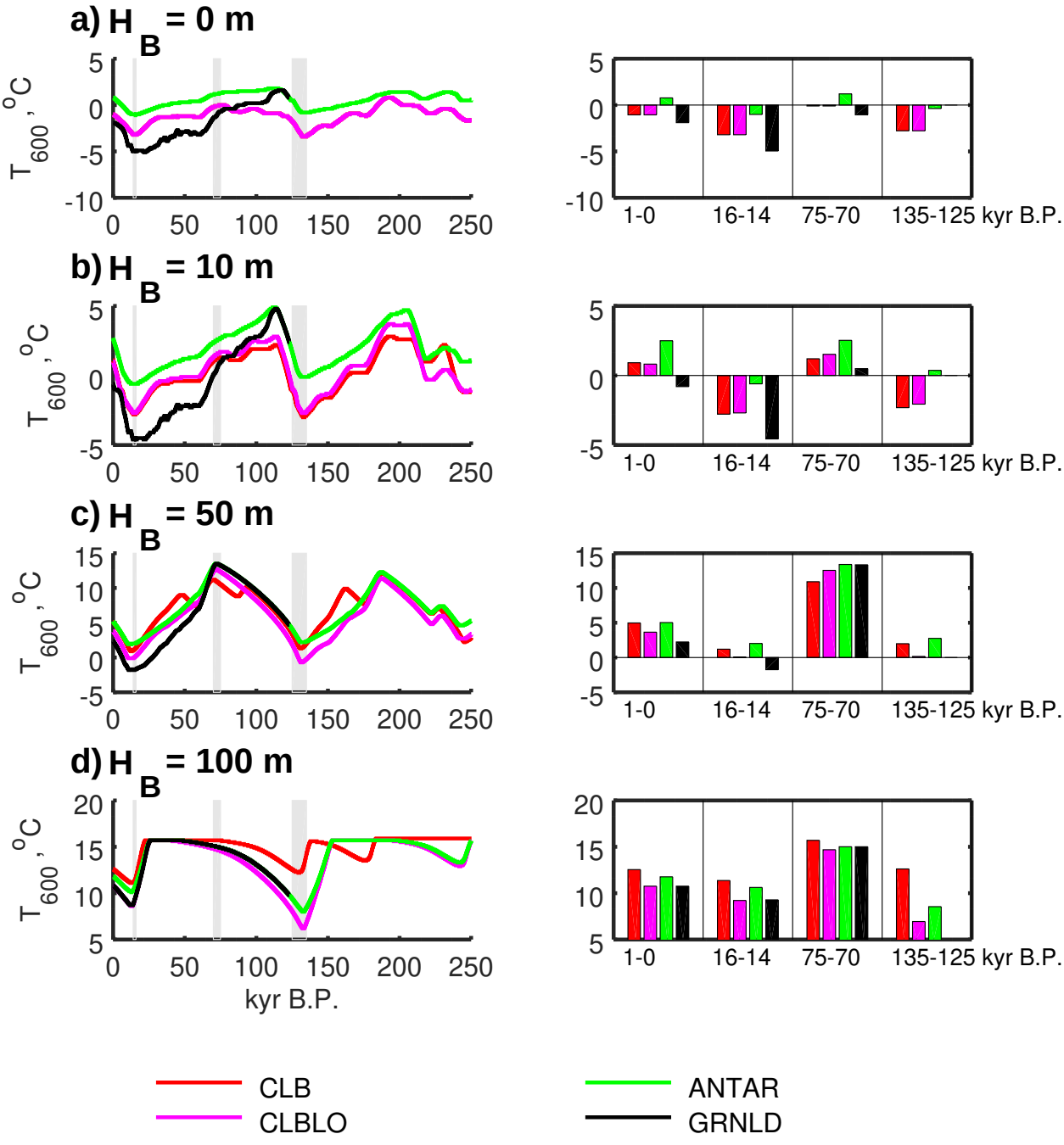

Fig. S5. Similar to Fig. 3 of the main text, but for the simulations with $G = 80\,\mathrm{mW\,m^{-2}}$.

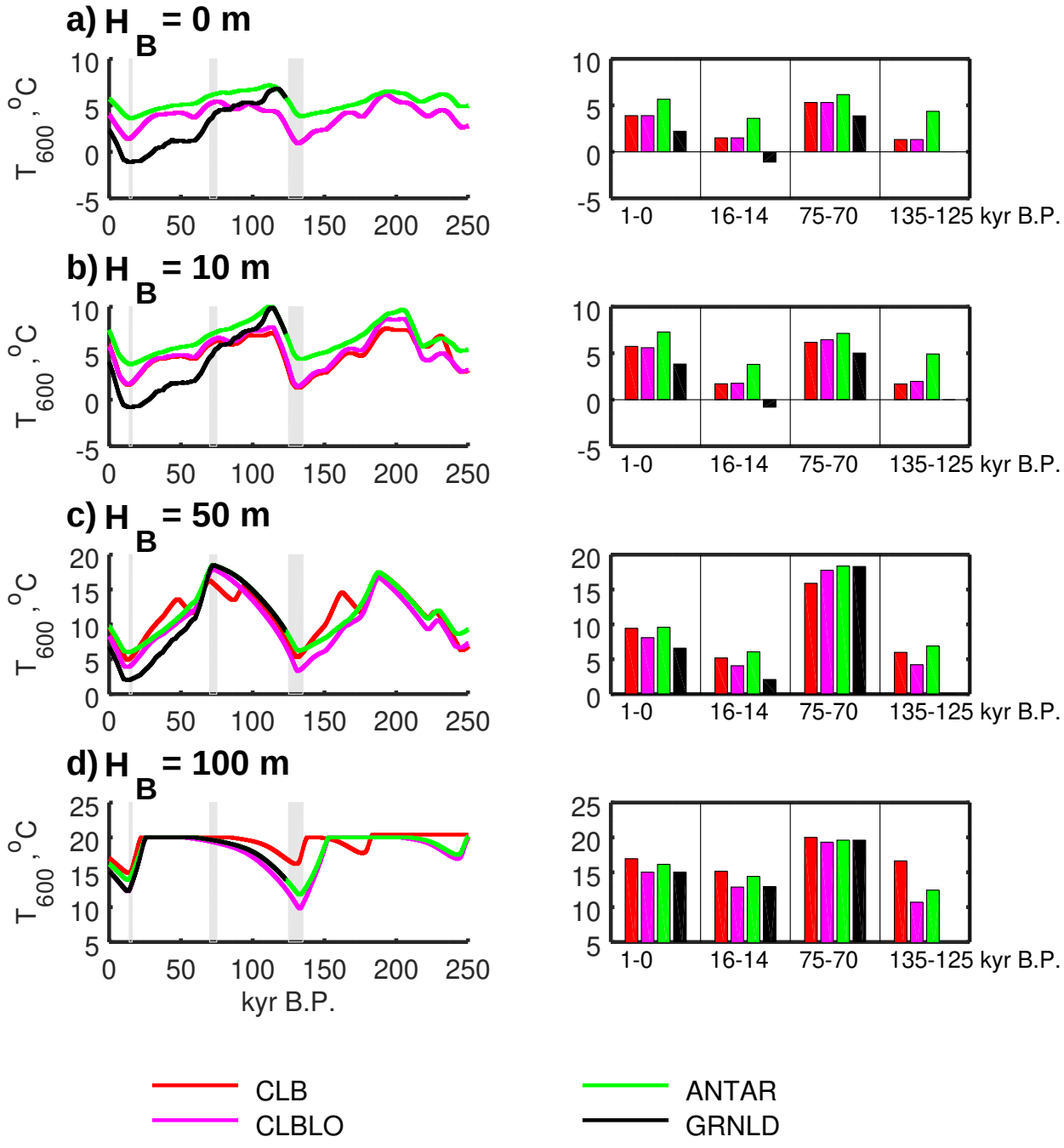

Fig. S6. Similar to Fig. 3 of the main text, but for the simulations with $G = 100\,\mathrm{mW\,m^{-2}}$.

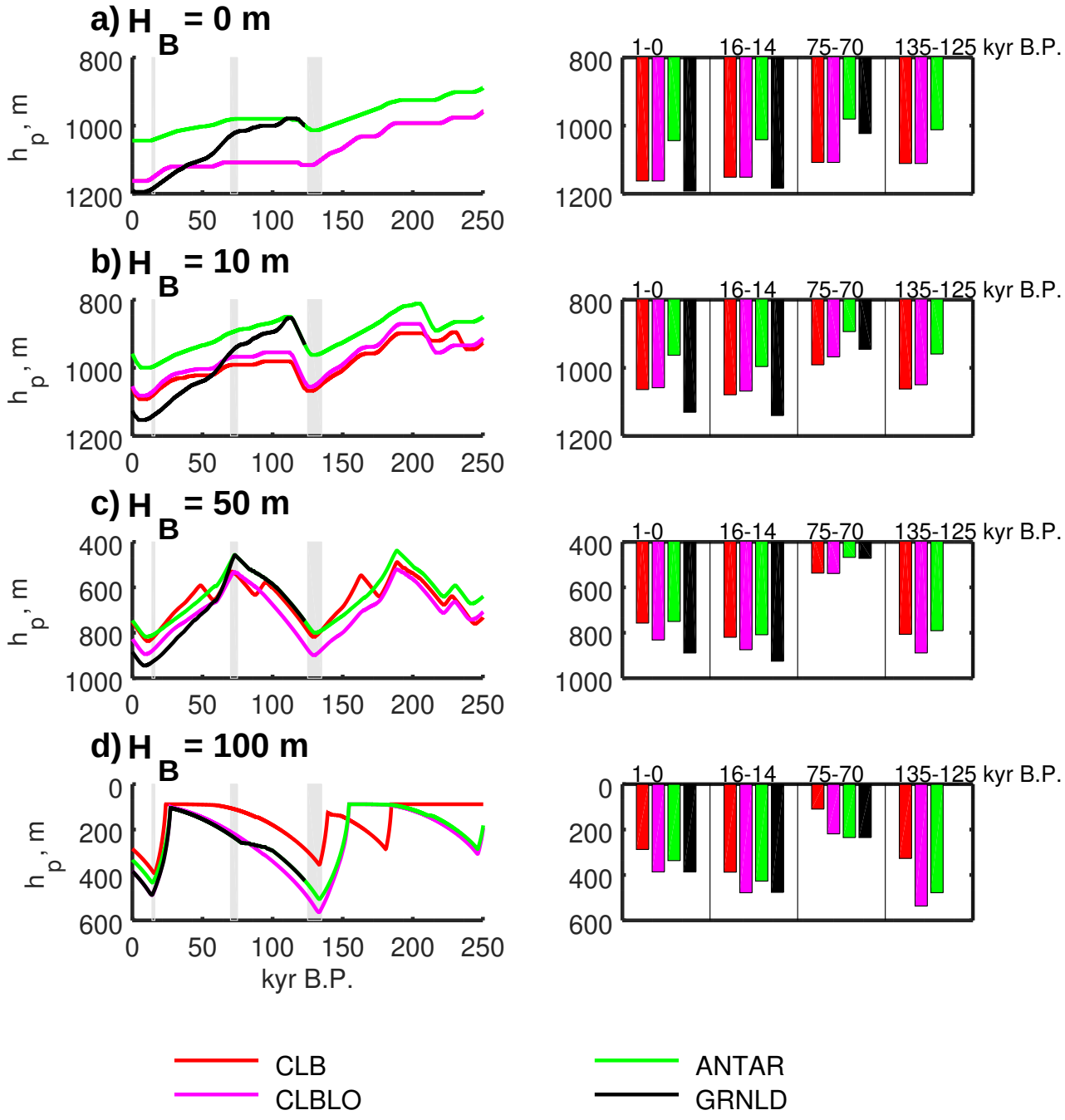

Fig. S7. Similar to Fig. 5 of the main text, but for the simulations with $G = 40\,\mathrm{mW\,m^{-2}}$.

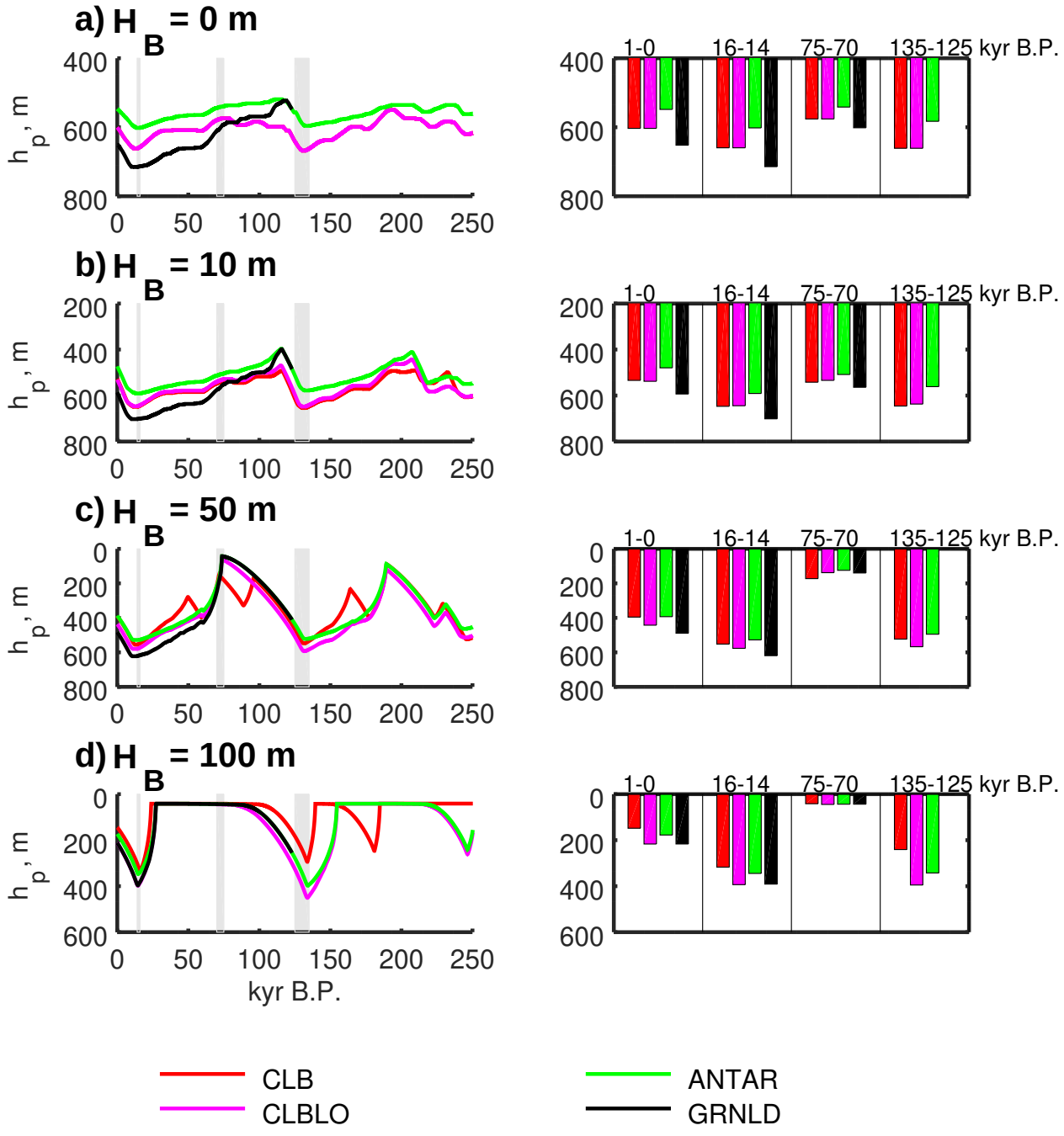

Fig. S8. Similar to Fig. 5 of the main text, but for the simulations with $G = 80\,\mathrm{mW\,m^{-2}}$.

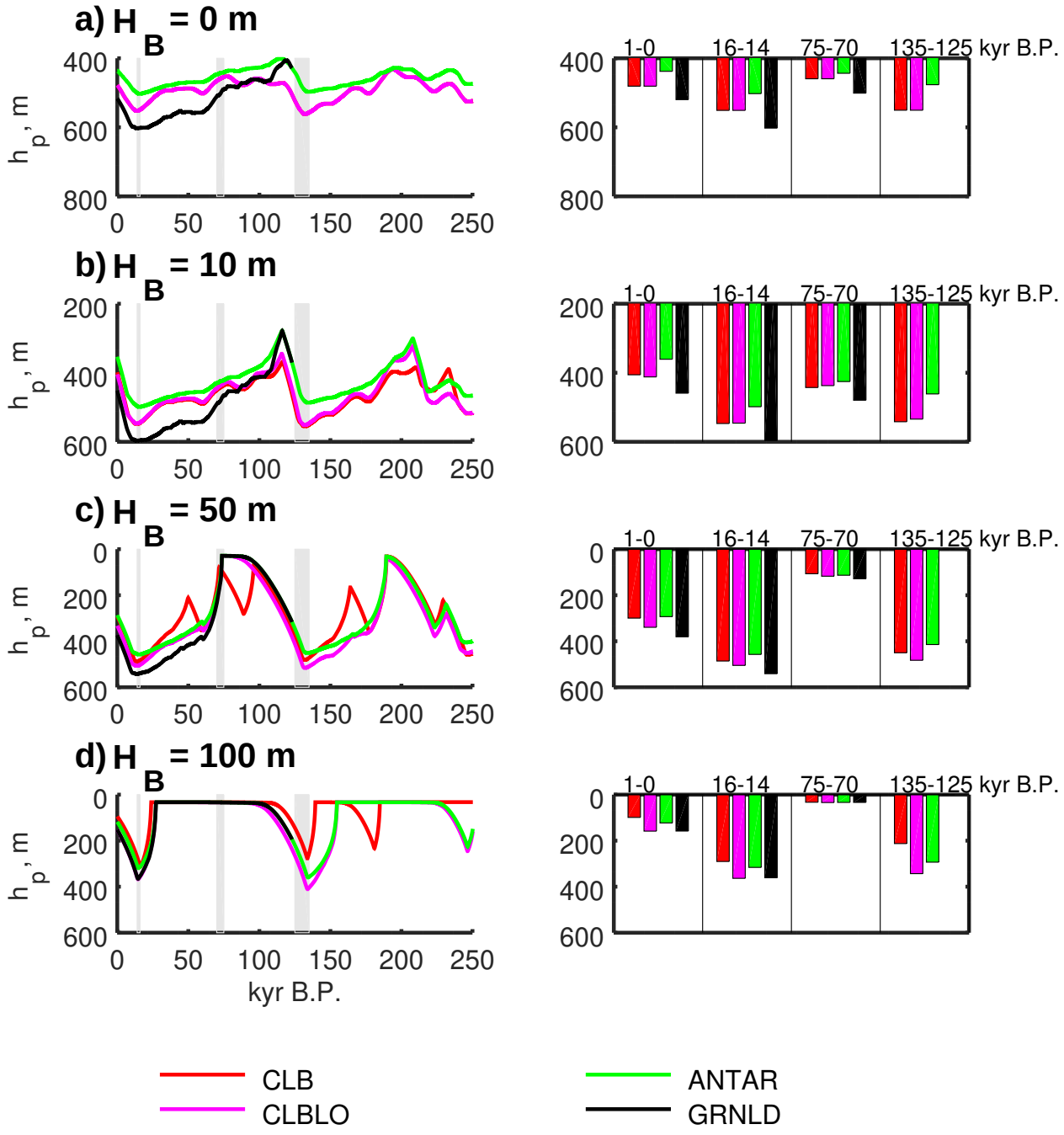

Fig. S9. Similar to Fig. 5 of the main text, but for the simulations with $G = 100\,\mathrm{mW\,m^{-2}}$.

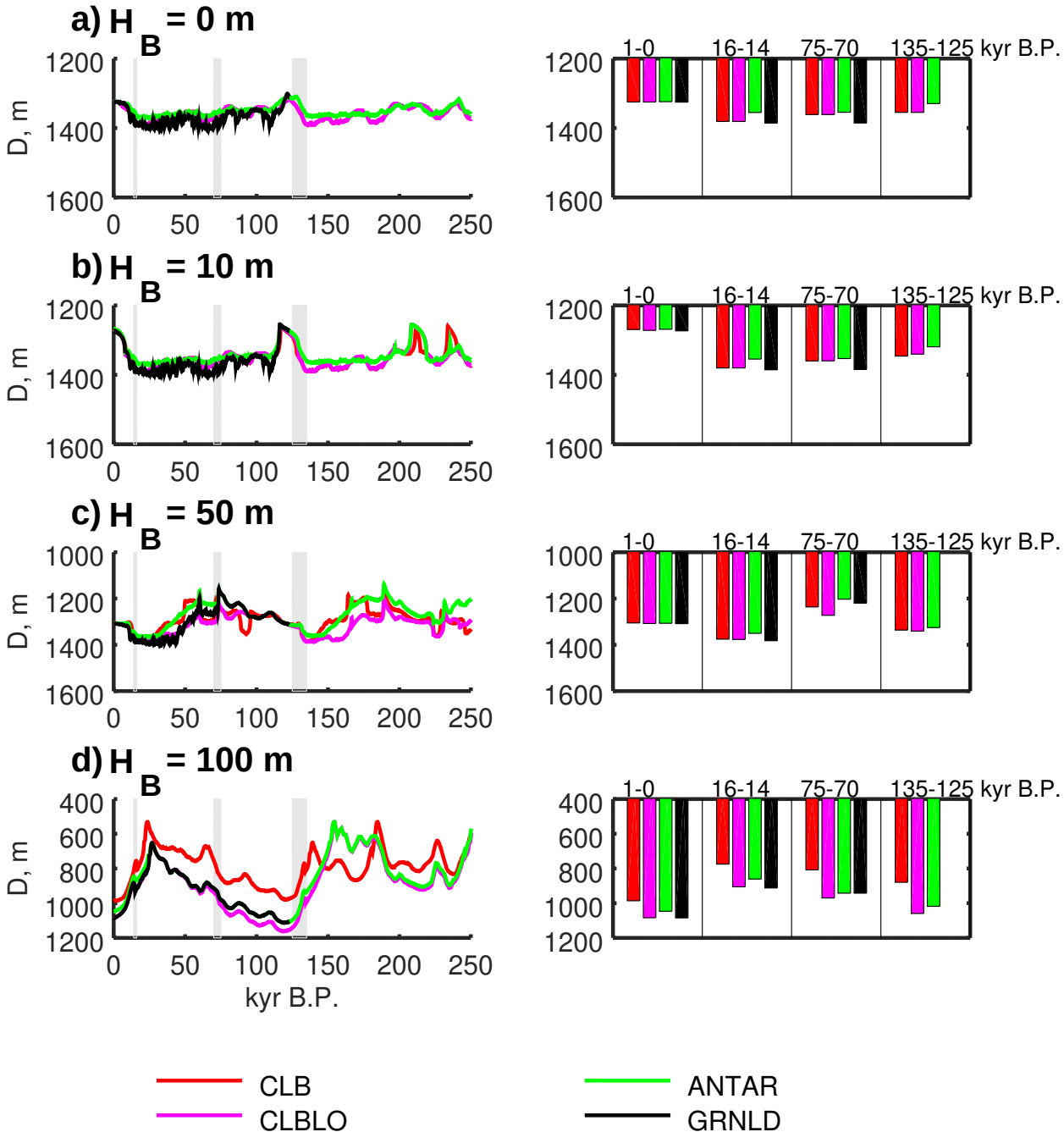

Fig. S10. Similar to Fig. 7 of the main text, but for the simulations with $G = 40\,\mathrm{mW\,m^{-2}}$.

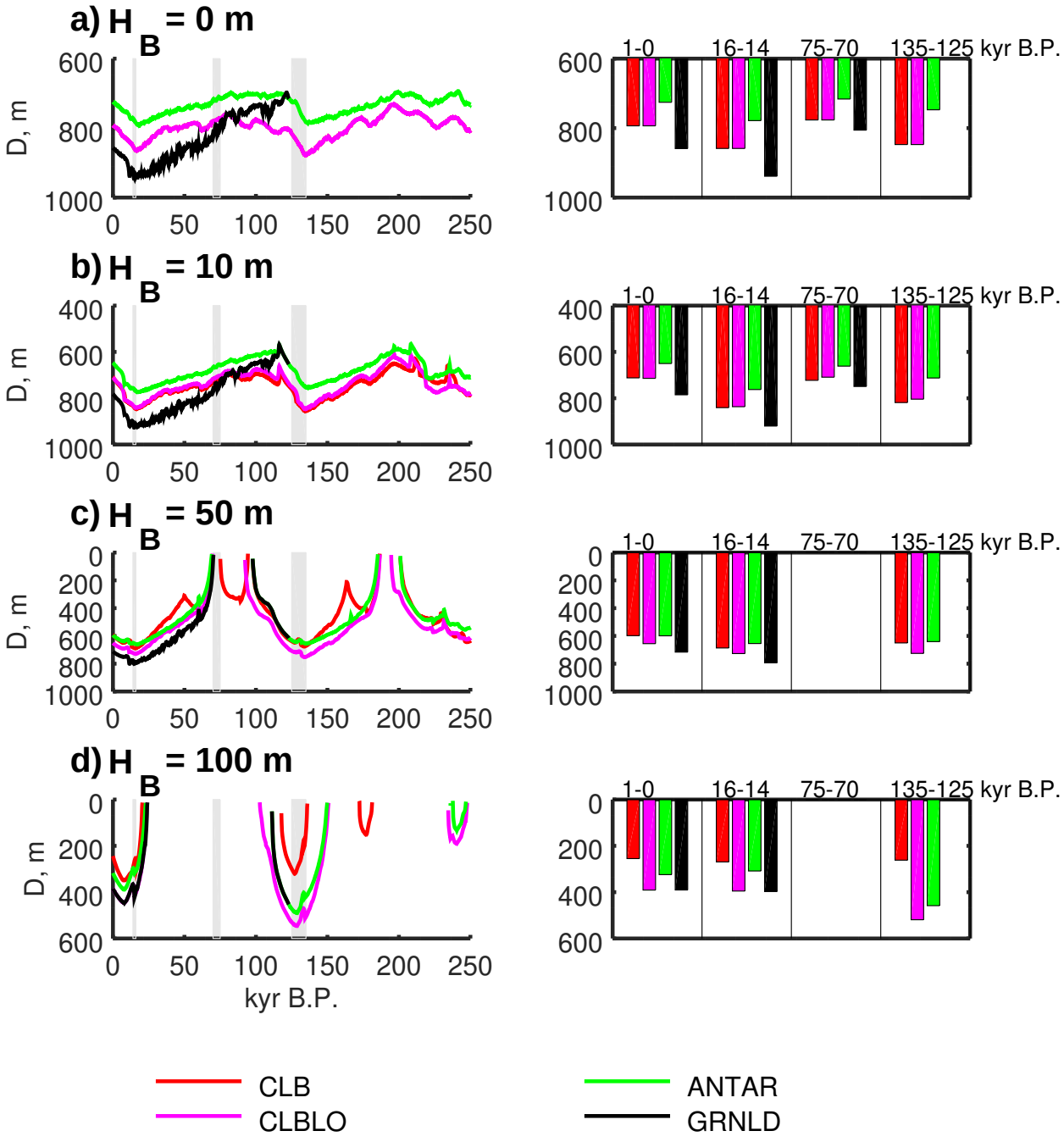

Fig. S11. Similar to Fig. 7 of the main text, but for the simulations with $G = 80\,\mathrm{mW\,m^{-2}}$.

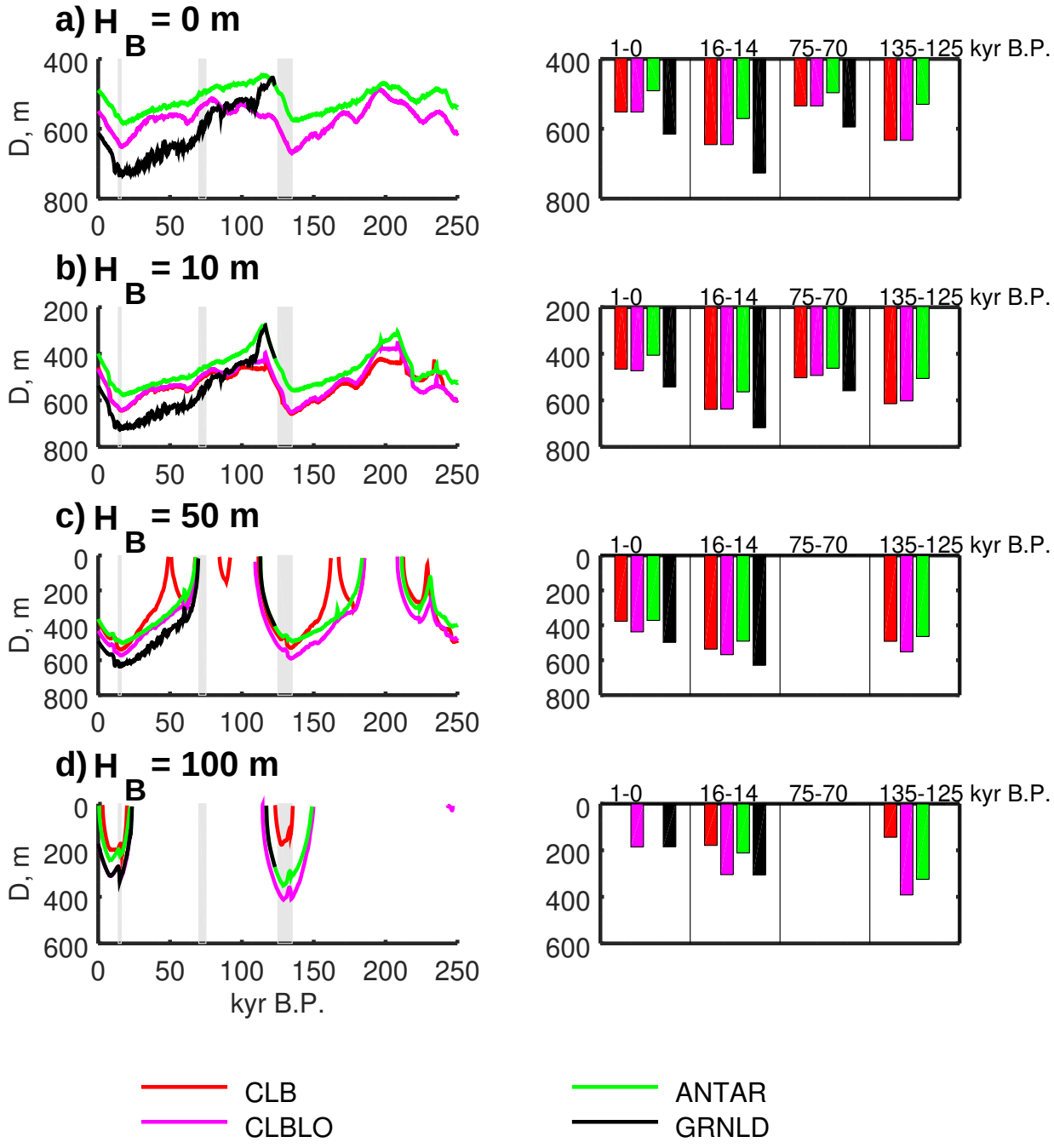

Fig. S12. Similar to Fig. 7 of the main text, but for the simulations with $G = 100\,\mathrm{mW\,m^{-2}}$.

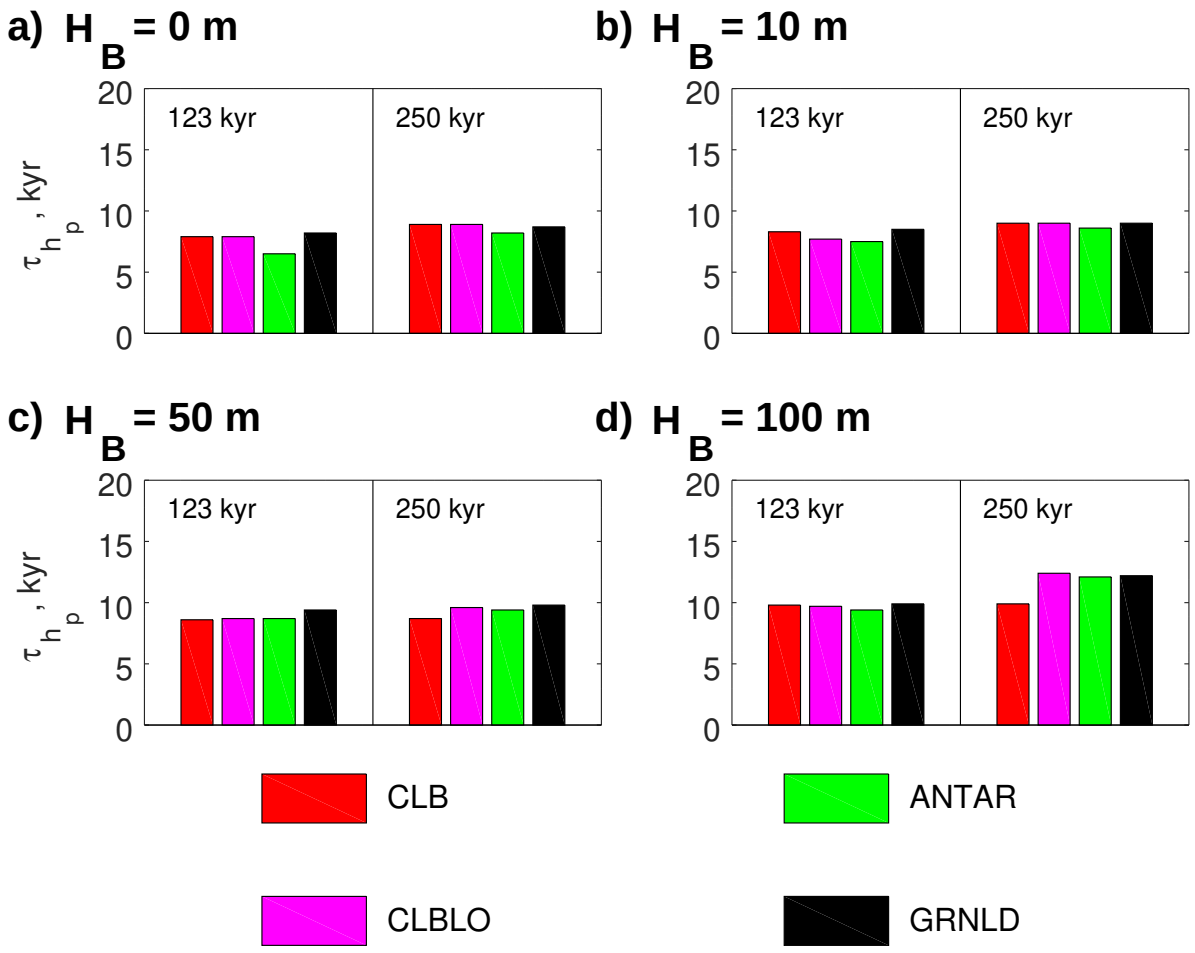

Fig. S13. Similar to Fig. 10 of the main text but for the simulations with $G = 40\,\mathrm{mW\,m^{-2}}$.

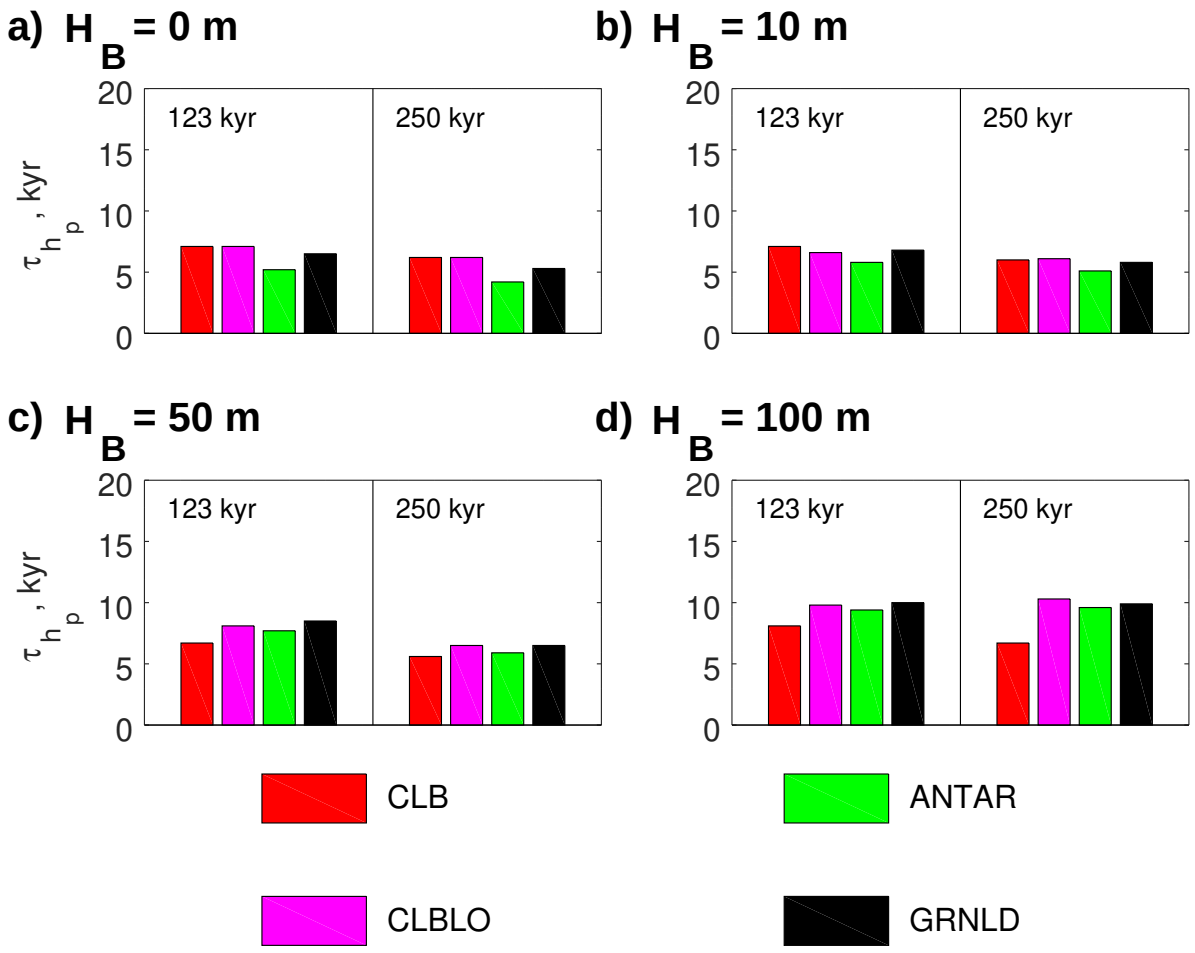

Fig. S14. Similar to Fig. 10 of the main text but for the simulations with $G = 100\,\mathrm{mW\,m^{-2}}$.

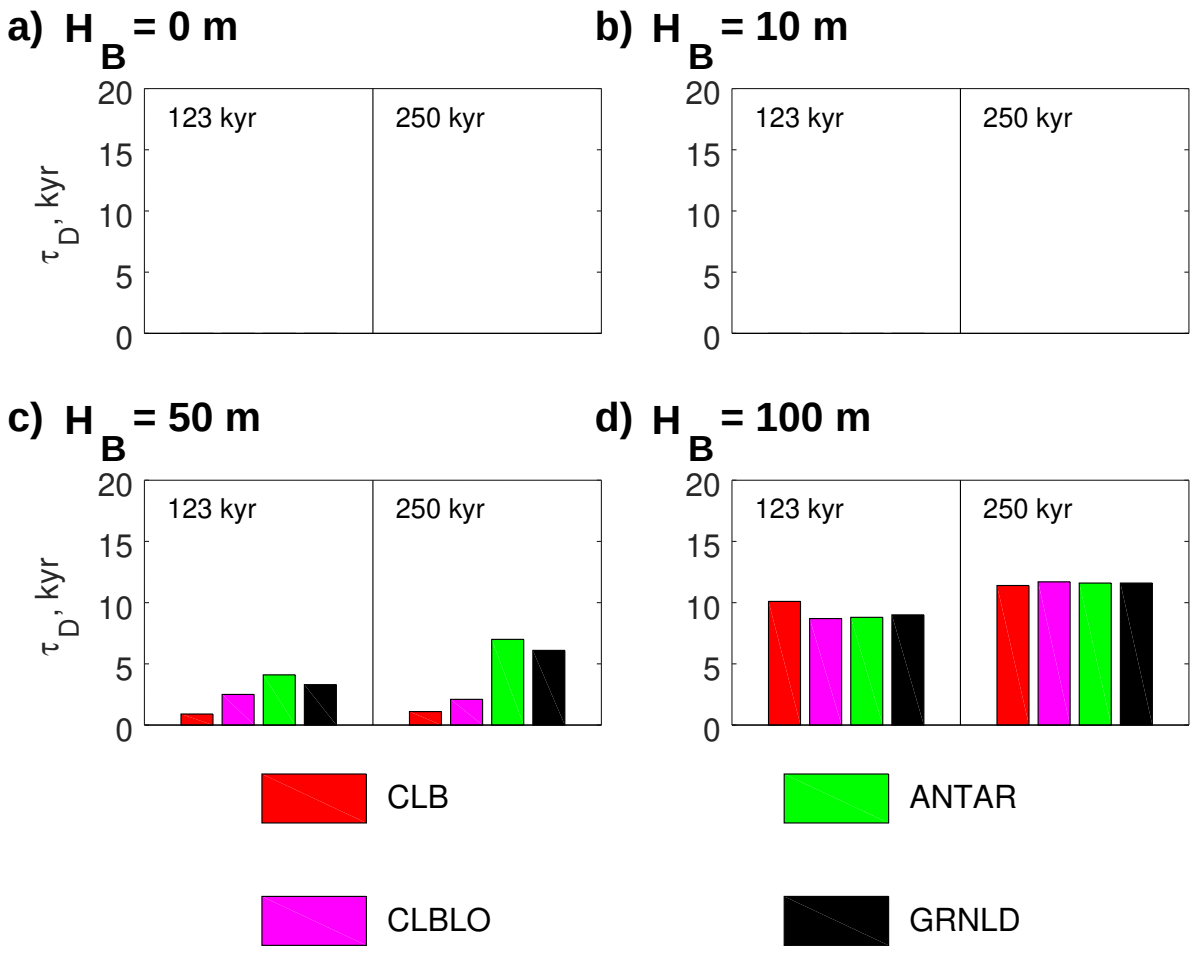

Fig. S15. Similar to Fig. 11 of the main text but for the simulations with $G = 40\,\mathrm{mW\,m^{-2}}$.

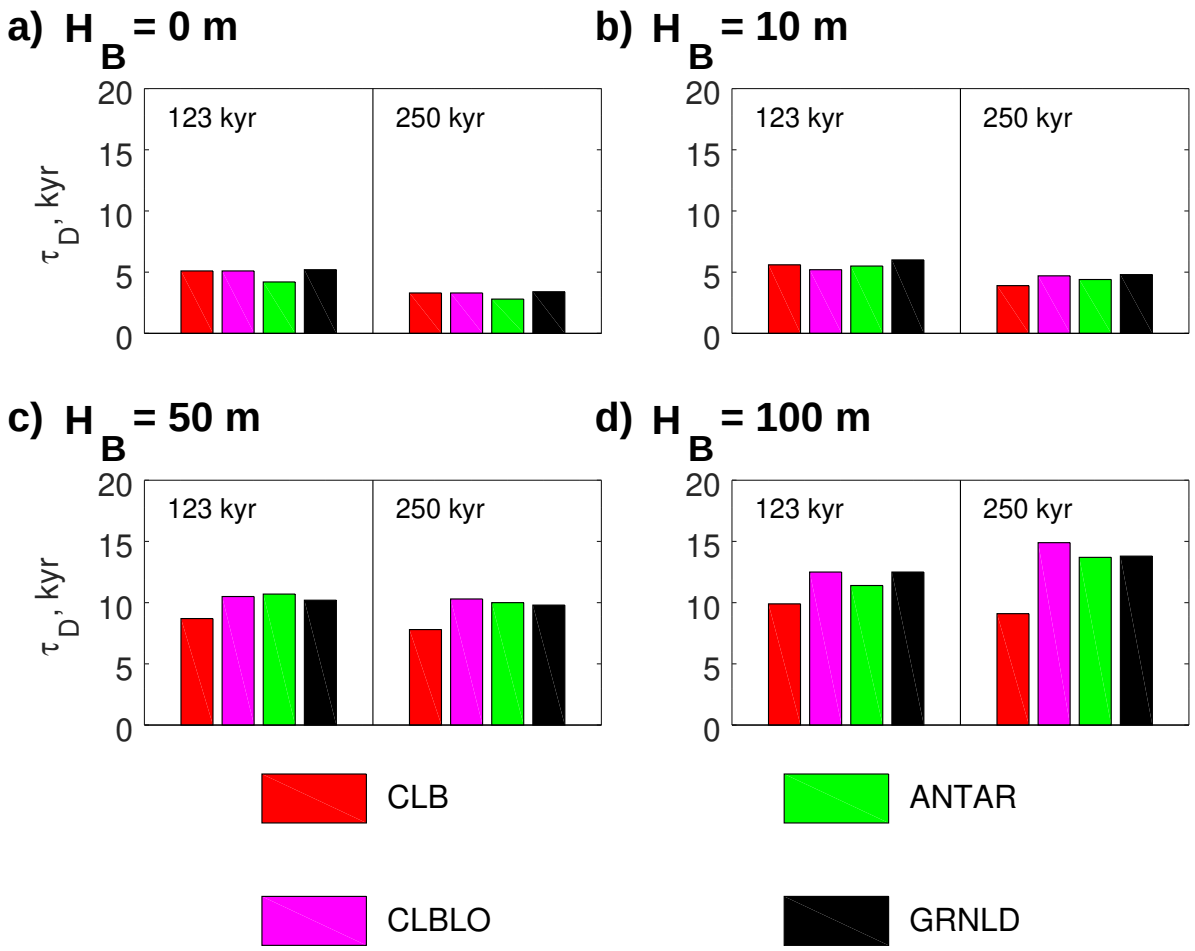

Fig. S16. Similar to Fig. 11 of the main text but for the simulations with $G = 100\,\mathrm{mW\,m^{-2}}$.

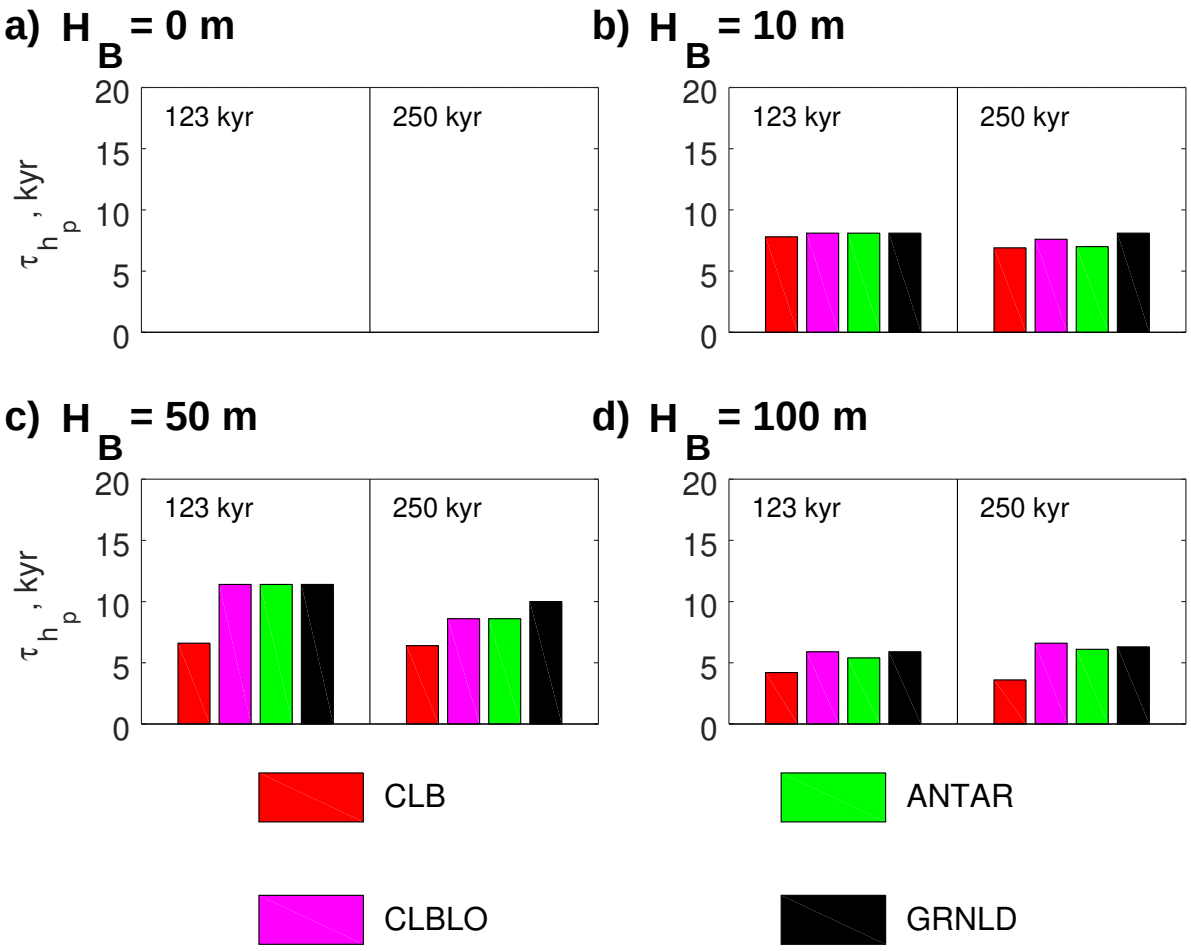

Fig. S17. Similar to Fig. 10 of the main text but with T_{B} in place of sea level.

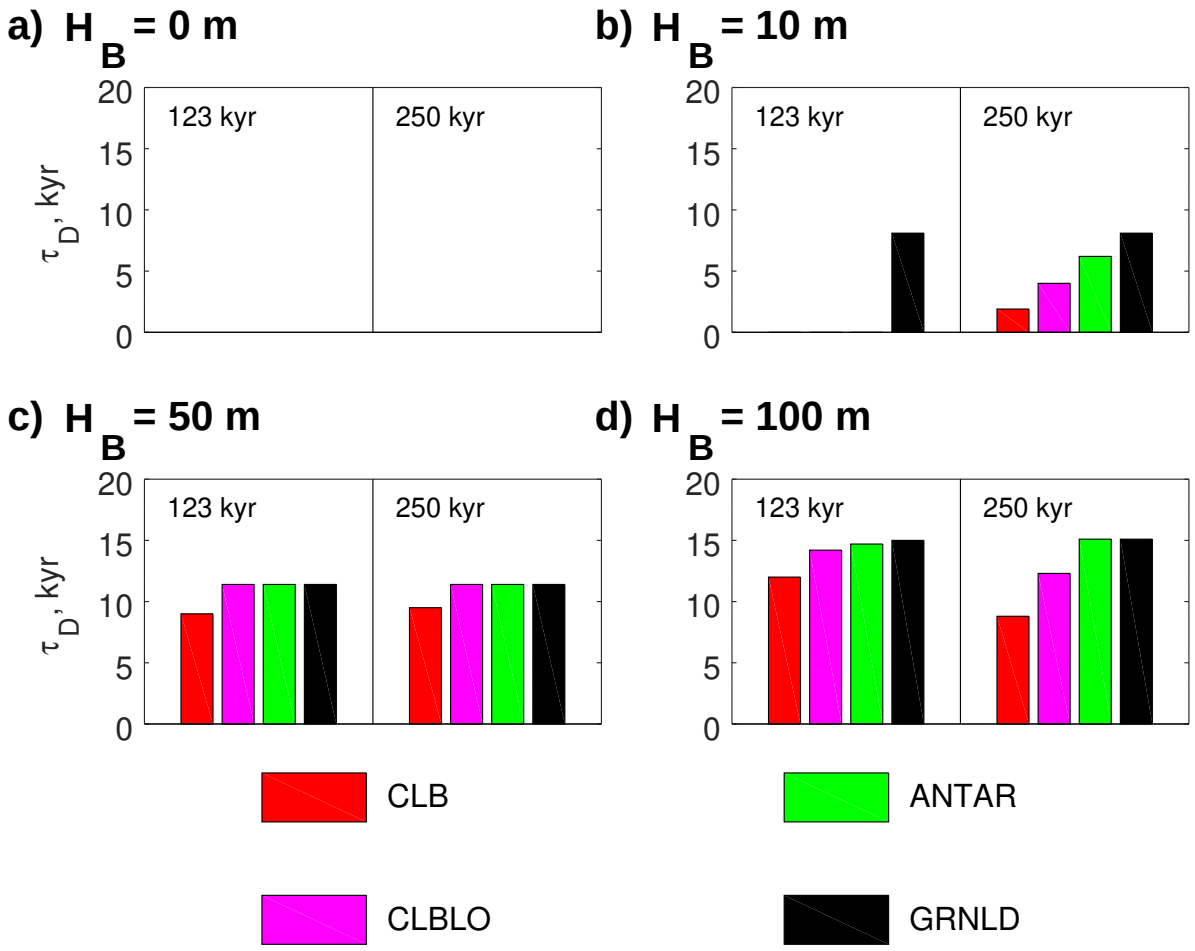

Fig. S18. Similar to Fig. 11 of the main text but with T_{B} in place of sea level.